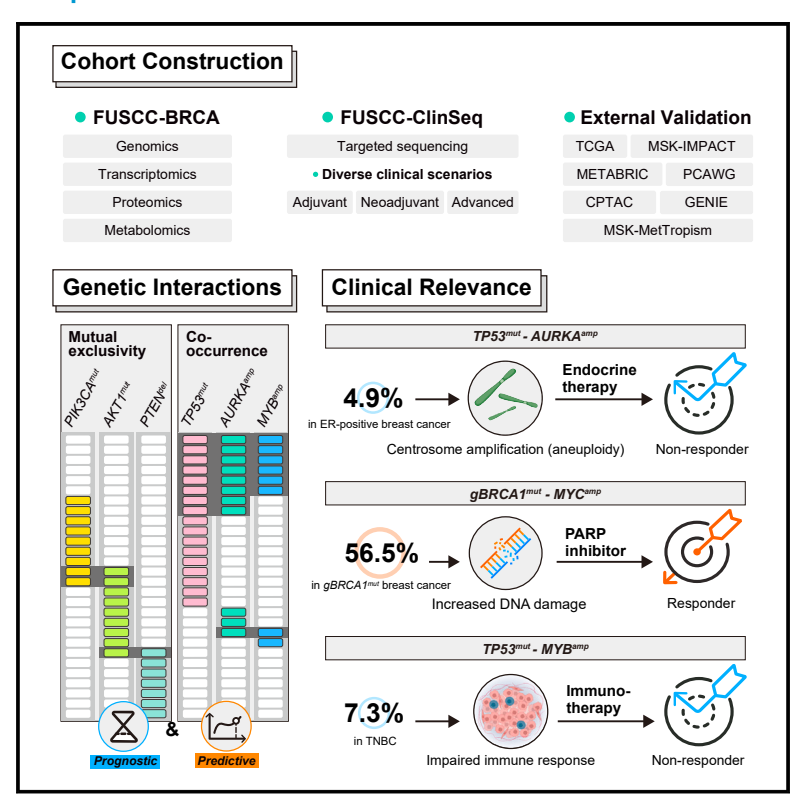
Genetic interactions reveal distinct biological and therapeutic implications in breast cancer

Graphical abstract



Authors

Cai-Jin Lin, Xi Jin, Ding Ma, ..., Xin Hu, Zhi-Ming Shao, Yi-Zhou Jiang

Correspondence

xinhu@fudan.edu.cn (X.H.), zhimingshao@fudan.edu.cn (Z.-M.S.), yizhoujiang@fudan.edu.cn (Y.-Z.J.)

In brief

Lin et al. leverage a large-scale multiomics cohort and a real-world clinical sequencing cohort to explore genetic interactions and their impact on treatment outcomes across various clinical scenarios in breast cancer. These findings underscore the importance of making genome-informed precision treatment decisions that consider individual driver alterations and beyond.

Highlights

- We built a large multi-omics cohort and a real-world clinical sequencing cohort
- A genetic interaction network involves co-occurring and mutually exclusive events
- Co-alterations influence treatment outcomes across diverse clinical scenarios
- Genome-informed treatment decisions should extend beyond single driver alterations







Article

Genetic interactions reveal distinct biological and therapeutic implications in breast cancer

Cai-Jin Lin, 1,3 Xi Jin, 1,3 Ding Ma, 1,3 Chao Chen, 1,3 Yang Ou-Yang, 1,3 Yu-Chen Pei, 2 Chao-Zheng Zhou, 1 Fei-Lin Qu, 1 Yun-Jin Wang,² Cheng-Lin Liu,¹ Lei Fan,¹ Xin Hu,^{2,*} Zhi-Ming Shao,^{1,*} and Yi-Zhou Jiang^{1,4,*}

1 Key Laboratory of Breast Cancer, Department of Breast Surgery, Fudan University Shanghai Cancer Center; Department of Oncology, Shanghai Medical College, Fudan University, Shanghai 200032, China

²Precision Cancer Medical Center, Fudan University Shanghai Cancer Center, Shanghai 200032, China

SUMMARY

Co-occurrence and mutual exclusivity of genomic alterations may reflect the existence of genetic interactions, potentially shaping distinct biological phenotypes and impacting therapeutic response in breast cancer. However, our understanding of them remains limited. Herein, we investigate a large-scale multi-omics cohort (n = 873) and a real-world clinical sequencing cohort (n = 4,405) including several clinical trials with detailed treatment outcomes and perform functional validation in patient-derived organoids, tumor fragments, and in vivo models. Through this comprehensive approach, we construct a network comprising co-alterations and mutually exclusive events and characterize their therapeutic potential and underlying biological basis. Notably, we identify associations between TP53^{mut}-AURKA^{amp} and endocrine therapy resistance, germline BRCA1mut-MYCamp and improved sensitivity to PARP inhibitors, and TP53mut-MYBamp and immunotherapy resistance. Furthermore, we reveal that precision treatment strategies informed by co-alterations hold promise to improve patient outcomes. Our study highlights the significance of genetic interactions in guiding genome-informed treatment decisions beyond single driver alterations.

INTRODUCTION

Precision oncology has revolutionized the therapeutic landscape in breast cancer by introducing new therapeutic options through the ongoing appreciation of cancer genomes and routine application of next-generation sequencing.¹⁻³ Genome-targeted or genomeinformed therapies, such as anti-ERBB2-targeted therapies or PARP inhibitors (PARPi), have improved outcomes in patients with specific genomic alterations. 4 While clinical success buoys efforts in precision treatment, efficacy remains limited due to the prevailing focus on single driver alterations in clinical decision-making, disregarding the impact of co-occurring genomic alterations on clinical outcomes. 5,6 Furthermore, the advent of promising agents such as immunotherapy complicates the accurate prediction of therapeutic responses, necessitating the identification of novel biomarkers beyond single driver alterations. Given these challenges, there is a compelling need to direct attention toward genetic interactions to effectively guide precision treatment.

Cancer initiation is orchestrated by the convergence of genetic alterations occurring sequentially within multiple genes, exhibiting non-random and regulated patterns.8 The observed cooccurrence or mutual exclusivity of these genetic alterations may reflect the existence of genetic interactions, thus delineating distinct functional relationships. Specifically, mutual exclusivity suggests either functional redundancy or antagonism, dictating synthetic lethal interactions with therapeutic potential in patients lacking targetable alterations.9 Conversely, co-occurrence reflects functional cooperation, 10 suggesting synthetic rescue interactions and possible resistance to treatment targeting one of the co-alterations. 11 Recent efforts have provided insights into non-random patterns of particular driver alterations. 12,13 Mutual exclusivity has been investigated across various tumor types, 12-17 while certain instances of co-occurring alterations have presented associations with clinical outcomes and microenvironment compositions. 10,18-24 CRISPR and compound screening have also provided evidence of the interplay between specific oncogenic alterations.^{25,26} Despite a growing focus on co-occurrence and mutual exclusivity, clinical consequences behind these events have not been fully elucidated.

Overall, ongoing new insights into cancer genome necessitate a focus on co-occurrence and mutual exclusivity of genomic alterations. To investigate their biological properties and discern the impact on treatment outcomes, we deliver a large-scale multi-omics cohort (FUSCC-BRCA) alongside a well-annotated prospective targeted sequencing cohort (FUSCC-ClinSeq). These findings may therefore improve our ability to explain variations in treatment response and complement ongoing efforts in precision oncology.



³These authors contributed equally

⁴Lead contact

^{*}Correspondence: xinhu@fudan.edu.cn (X.H.), zhimingshao@fudan.edu.cn (Z.-M.S.), yizhoujiang@fudan.edu.cn (Y.-Z.J.) https://doi.org/10.1016/j.ccell.2024.03.006



RESULTS

Patient samples, clinical data, and study cohorts

To systematically explore the underlying biology and clinical relevance of co-occurring and mutually exclusive genomic alterations, we established a large-scale multi-omics cohort, namely, the FUSCC-BRCA cohort, and a prospective clinical sequencing cohort, namely, the FUSCC-ClinSeq cohort.

FUSCC-BRCA features multi-omics data, clinicopathological details, and clinical outcomes of 873 Asian breast cancer patients (Figure 1; Table S1). All 873 patients had both wholeexome sequencing data on primary tumor tissues and paired blood samples and somatic copy number alteration (CNA) data; 842 patients had RNA sequencing data; 261 patients had tandem mass tags-based mass spectrometry quantified protein data; and 509 patients had metabolomic data. We used this cohort to identify co-occurrence and mutual exclusivity of genomic alterations, investigate their interactions with treatment, and characterize their molecular biology according to detailed annotation and complete omics data.

FUSCC-ClinSeq represents a prospective cohort of targeted sequencing on matched tumor and blood samples from 4,405 Asian breast cancer patients, with detailed treatment records. Notably, this cohort encompasses several clinical trials such as NCT04613674, NCT03805399, NCT04395989, NCT04355858, and NCT04129996. There were three subcohorts (Figure 1; Table S1): 2,418 early-stage patients receiving surgery and adjuvant therapy, 1,373 locally advanced patients undergoing neoadjuvant therapy followed by surgery, and 614 advanced patients receiving salvage treatment. This cohort was used to investigate co-occurrence and mutual exclusivity involving germline alterations and explore their therapeutic impact.

To comprehensively interpret the co-occurrences and mutual exclusivities, we also included TCGA-BRCA (n = 983), MSK-IMPACT (n = 1,918), METABRIC (n = 2,509), AACR Project GENIE (n = 13,308), MSK-MetTropism (pan-cancer; n = 25,775), PCAWG (pan-cancer; n = 2,922), and CPTAC breast cancer (n = 122) cohorts for external validation and biological characterization (Figure 1). The clinicopathological features of different cohorts were summarized in Table S1. Furthermore, we established a drug-testing platform containing patient-derived organoids (PDOs), tumor fragments (PDTFs), and in vivo xenografts or isografts for functional validation (Figure 1; Table S1).

Collectively, we established a multi-omics cohort, a clinical sequencing cohort, and a drug-testing platform, together with multiple external cohorts, to systematically characterize the underlying biology and clinical relevance of co-occurring and mutually exclusive genetic events.

Molecular landscape of the FUSCC-BRCA cohort

We present a well-annotated landscape of the FUSCC-BRCA cohort (Figure 2A). Consistent with previous studies, 27,28 the prevalent genetic alterations in breast cancer included TP53 alterations (47.8%), PIK3CA alterations (37.7%), and MYC amplifications (19.5%). The distribution of genomic alterations varied among different clinical subtypes, with TP53 alterations occurring in 78.4% of triple-negative breast cancers (TNBC) and ERBB2 alterations being most frequent in HER2-positive breast cancer (85.0% in HR+HER2+ and 80.6% in HR-HER2+ subtypes).

We then investigated the differences in the genome profiles of the FUSCC-BRCA cohort with TCGA cohort (Figure S1A; Table S2). Notable differences include lower occurrences of CDH1 mutation (3.6% in FUSCC-BRCA versus 17.9% in TCGA Caucasians; FDR < 0.001) and higher occurrences of TP53 mutation (26.5% in FUSCC-BRCA versus 17.1% in TCGA Caucasians; FDR = 0.006), AKT1 mutation (7.6% in FUSCC-BRCA versus 3.4% in TCGA Caucasians; FDR = 0.035), and PIK3CA amplifications (7.6% in FUSCC-BRCA versus 2.1% in TCGA Caucasians; FDR = 0.004) in HR+HER2- subtype, as well as higher prevalence of ERBB2 amplifications (82.4% in FUSCC-BRCA versus 51.3% in TCGA Caucasians; FDR < 0.001) in HER2+ subtype. Collectively, we presented a comprehensive landscape and highlighted the racial disparities in genomic alterations in Asian patients with breast cancer.

Selection of cancer driver genes and functional alterations

Before identifying co-occurrences and mutual exclusivities, we compiled a list of cancer driver genes, including 457 oncogenes, 477 tumor suppressor genes, and 75 cancer predisposition genes (Figure S1B; Table S3). Utilizing dNdScv and MutSigCV (Table S3), we identified four additional significantly mutated genes in the FUSCC-BRCA cohort, namely, AMY2A, ZFPM1, RBMXL2, and SOX10, which were also integrated into the cancer driver gene list. In the FUSCC-BRCA cohort, HR+HER2- tumors presented higher mutation frequencies in AMY2A, RBMXL2, and ZFPM1 compared to TCGA Caucasians, with no notable difference observed in SOX10 (Figure S1C). Further external validations are necessary to confirm the observed difference.

We then retained the somatic oncogenic alterations and germline pathogenic/likely pathogenic variants for functional interpretation of co-occurrences and mutual exclusivities. For CNAs, we concentrated on actionable CNAs at the gene level rather than at the region of interest level for clinical interpretability (Table S3). We incorporated the functional alterations of the cancer driver genes for the discovery of co-occurrences and mutual exclusivities (Figure 2A; Table S3).

Network construction of co-occurrences and mutual exclusivities

To infer interactions between functional alterations, we performed Selected Events Linked By Evolutionary Conditions Across Human Tumors (SELECT)^{12,13} analysis within the entire FUSCC-BRCA cohort accounting for breast cancer subtypes and within individual clinical subtypes. The resulting network comprised 50 co-occurring events and 30 mutually exclusive events (Figure 2B; Table S3). Validated known events included the co-occurrence of TP53 mutation and MYC amplification and the mutual exclusivity of PIK3CA and AKT1 mutations. 11 Additionally, we also identified events previously unreported, such as co-occurring TP53^{mut}-MYB^{amp}. For germline variants, only the co-occurring gBRCA1mut-MYCamp was found due to the low prevalence and limited FUSCC-BRCA cohort size. Therefore, we performed SELECT analysis within the FUSCC-ClinSeq cohort separately and found additional 4 co-alterations and 8 mutually exclusive alterations involving germline variants, such as the co-occurring gBRCA1^{mut}-TP53^{mut} and the mutually exclusive gBRCA2mut-gPALB2mut (Figure S2A).



Network Construction MSK-IMPACT Genomics FUSCC-ClinSeq **Transcriptomics** WES **CPTAC** (N = 873)RNA-seq TCGA OncoScan **GENIE** (N = 842)(N = 873)**METABRIC** Metabolomics **Proteomics** MSK-MetTropism **PCAWG** Lipidome (N = 509) Protein **FUSCC-BRCA** Co-Occurrence External (N = 261)**Validation** & Mutual Exclusivity **Clinical Validation Multi-Omics Analysis Mechanistic Exploration Adjuvant** N = 2,418Genomic alterations Copy number signature Neoadjuvant N = 1.373Chromosome instability Advanced N = 614Organoid Genomic properties FUSCC-ClinSeq CDK4/6 inhibitor **Anthracycline-Taxane Anti-PD1 Trastuzumab** Tyrosine kinase inhibitor PARP inhibitor Upregulated Aromatase inhibitor **Tumor fragment** Downregulated Downstream pathway changes Treatment record Capsulize Transplant Amino acid Other Peptide Carbohydrates **CO-ALTERATION** Lipid Vitamins and Cofactors ÷ Xenobiotics Nucleotide Mini-PDX Polar metabolites Fatty acyls [FA] Sphingolipids [SP] -D Glycerolipids [GL] Sterol Lipids [ST] Glycerophospholipids [GP] Lipids **Prognostic** and **Predictive** Clinical relevance Metabolic reprogramming Xenograft

Figure 1. Schematic overview of the study design See also Table \$1.



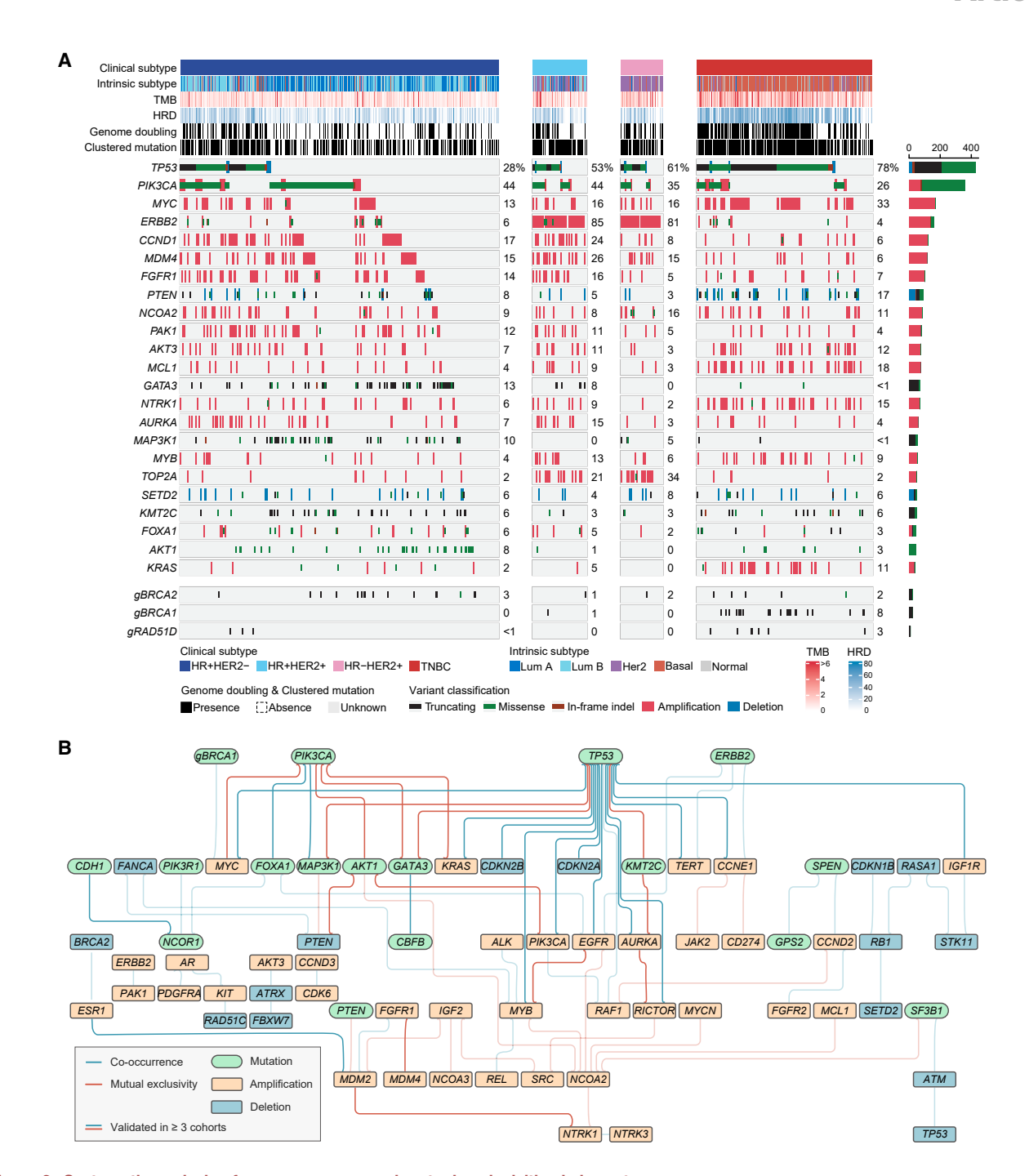


Figure 2. Systematic analysis of co-occurrences and mutual exclusivities in breast cancer

(A) Molecular landscape of the study cohort.

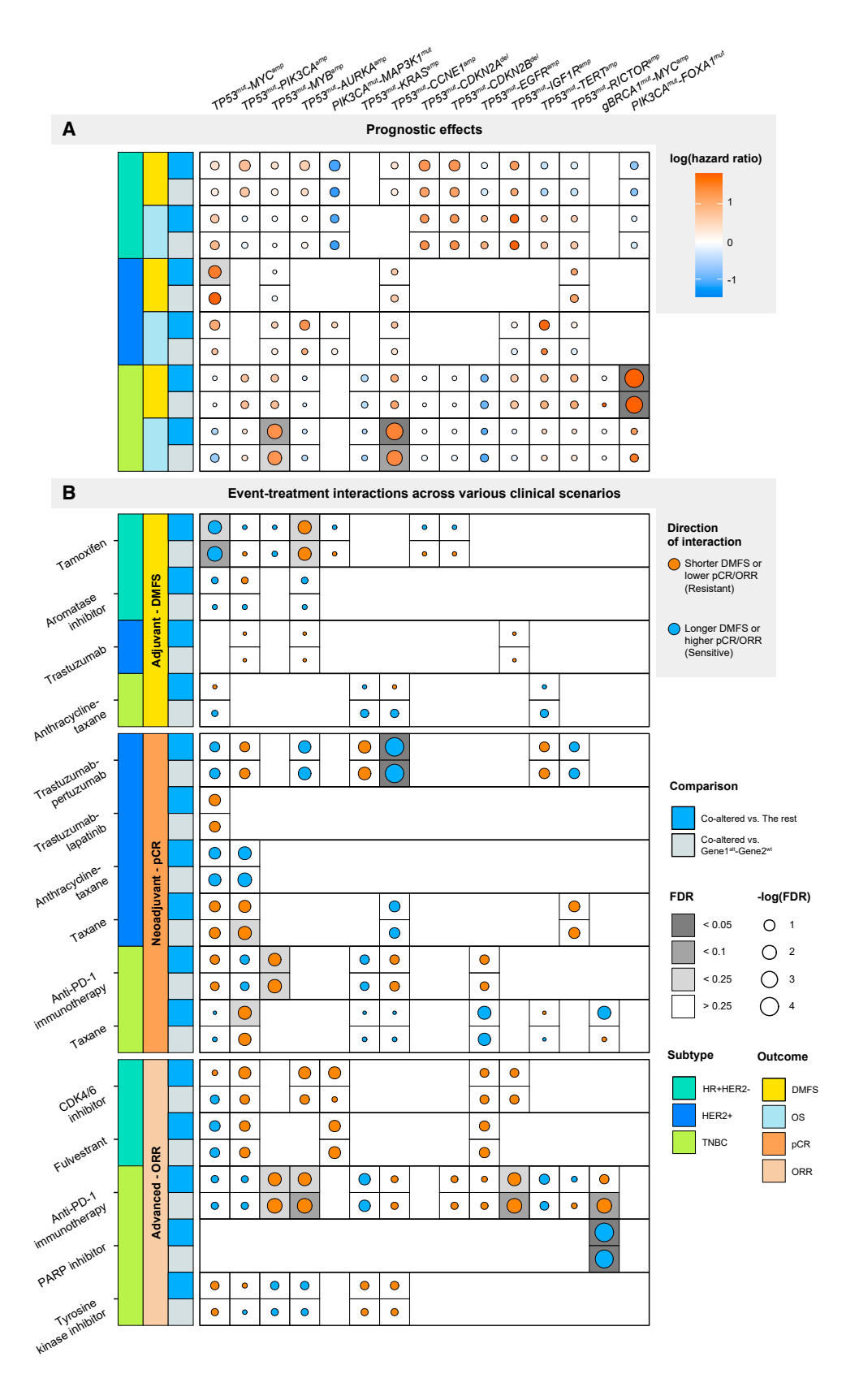
(B) Networks of co-occurring and mutually exclusive genomic alterations. See also Figures S1-S4 and Tables S2-S4.

We also created a network involving hotspot mutations (Figure S2B). Interestingly, despite global mutual exclusivity in the PI3K pathway, co-occurrence between PIK3CA.E542 and PIK3-CA.E726 was observed, which was associated with increased oncogenicity and sensitivity to PI3Kα inhibitors.²⁹

To interpret the associations with breast cancer subtypes, we compared co-alteration frequencies across different clinical and intrinsic subtypes. Significant differences were observed for most events (Figures S2C and S2D). For example, TP53mut-MYC^{amp} and TP53^{mut}-KRAS^{amp} were more prevalent in TNBCs or the basal-like subtype, while PIK3CAmut-MAP3K1mut was more common in HR+HER2- breast cancers and the luminal A subtype.

We then focused on racial disparities and compared the frequency of each co-alteration between FUSCC-BRCA and TCGA Caucasians or African Americans (Figure S2E). After





(legend on next page)



adjusting for the differential incidence of individual alterations, we observed higher incidence of co-occurring TP53mut-KRASamp within TNBCs when comparing FUSCC-BRCA with TCGA Caucasians (10.4% in FUSCC-BRCA versus 3.3% in TCGA Caucasians; p = 0.042).

Overall, our network highlights co-occurrence and mutual exclusivity patterns in breast cancer and reveals subtype-specific and race/ethnicity-specific distributions.

Validation of co-occurrences and mutual exclusivities in independent cohorts

To validate the co-occurrences and mutual exclusivities, we performed SELECT analysis across multiple cohorts, including FUSCC-ClinSeq, TCGA-BRCA, MSK-IMPACT, METABRIC, GENIE, MSK-MetTropism (pan-cancer), and PCAWG (pan-cancer) cohorts. Notably, 65.0% (52 out of 80) of the co-occurring and mutually exclusive events were validated in at least one independent cohort, and 38.8% (31 out of 80) of these events were validated in at least three cohorts. In addition, we further complemented the validation by literature review. Overall, a total of 68.8% (55 out of 80) of the events were validated in at least one independent cohort or through a literature review (Table S4).

To confirm the biological interactions rather than a random statistical estimation, we first investigated Euclidean distance to discern the global diversity in transcriptomic properties and polar and lipid metabolism. Our analysis indicated that coaltered tumors presented the most significant diversity in these aspects (Figure S3), highlighting the distinct biological basis among tumors with and without co-alterations. Subsequently, clonality analysis revealed that 92.9% (593 out of 638) of the co-occurring genomic alterations indeed occurred within a shared clone (Figure S4A), further supporting potential biological interactions between the co-occurring events. Additionally, we mapped the validated co-occurrences and mutual exclusivities onto the IntAct protein-protein interactome. Proteins presenting co-occurring interactions shared more interactors (nodes) than those of mutually exclusive interactions (Figure S4B), indicating potential functional synergy in specific biological processes. For example, BRCA1 and MYC share 44 interactors and enrichment analysis of these interactors suggested a functional collaboration in DNA repair pathways (Figures S4C and S4D). Similarly, TP53 and AURKA share 13 interactors, which were enriched in cell cycle pathways (Figures S4E and S4F). Taken together, we statistically and biologically validated the co-occurrences and mutual exclusivities and suggested potential functional interactions in specific biological processes.

Co-alterations are associated with treatment outcomes

To provide further insight into co-alterations, we associated these genomic events with patient survival and treatment outcomes (Figure 1). Our primary focus was on the prognostic effects of co-alterations with frequencies exceeding 1% on distant metastasis-free survival (DMFS) and overall survival (OS) (Figure 3A; Table S5). Based on a multivariate Cox proportional hazards model adjusting for baseline factors of age, histology, tumor size, and lymph node status, we observed that co-occurring PIK3CA^{mut}-FOXA1^{mut} was associated with poorer DMFS, while both TP53^{mut}-MYB^{amp} and TP53^{mut}-CCNE1^{amp} were indicative of worse OS within the TNBC subtype.

Furthermore, we investigated co-occurring alterations that might predict treatment response in adjuvant, neoadjuvant, and advanced settings per subtypes (Figure 3B; Table S5). In addition to prognostic effects generally associated with patient outcomes, this investigation aimed to determine the efficacy of a particular treatment for patients with and without a specific co-alteration. Specifically, within the HR+HER2- subtype, we found that TP53mut-AURKAmp carriers treated with adjuvant tamoxifen exhibited a higher risk of distant metastasis than noncarriers did, while TP53mut-MYCamp carriers demonstrated a more favorable response. Among HER2+ patients, the co-occurring TP53mut-CCNE1amp was associated with a higher likelihood of achieving a pathologic complete response (pCR) when treated with neoadjuvant trastuzumab-pertuzumab combinations. For TNBCs, the co-occurring TP53^{mut}-MYB^{amp} correlated with inferior immunotherapy efficacy in both the neoadjuvant and advanced settings. In addition, advanced gBRCA1^{mut}-MYC^{amp} carriers exhibited an increased objective response rate (ORR) to PARPi.

Collectively, we provided an overview of the association between co-alterations and treatment responses in diverse settings. These findings may help extend clinical interpretation and application of next-generation sequencing for optimized therapeutic benefit.

TP53^{mut}-AURKA^{amp} indicates endocrine resistance in the HR+HER2- subtype

Initial analysis revealed an interaction between co-alterations and treatment outcomes, warranting in-depth investigation into their biological basis. For clinically relevant co-occurring events, specifically the co-occurring TP53^{mut}-AURKA^{amp}, gBRCA1^{mut}-MYC^{amp}, and TP53^{mut}-MYB^{amp}, we deployed a comprehensive validation strategy encompassing diverse methodologies, including clinical validation, multi-omics analyses, and functional validation with mechanistic exploration (Figure 1).

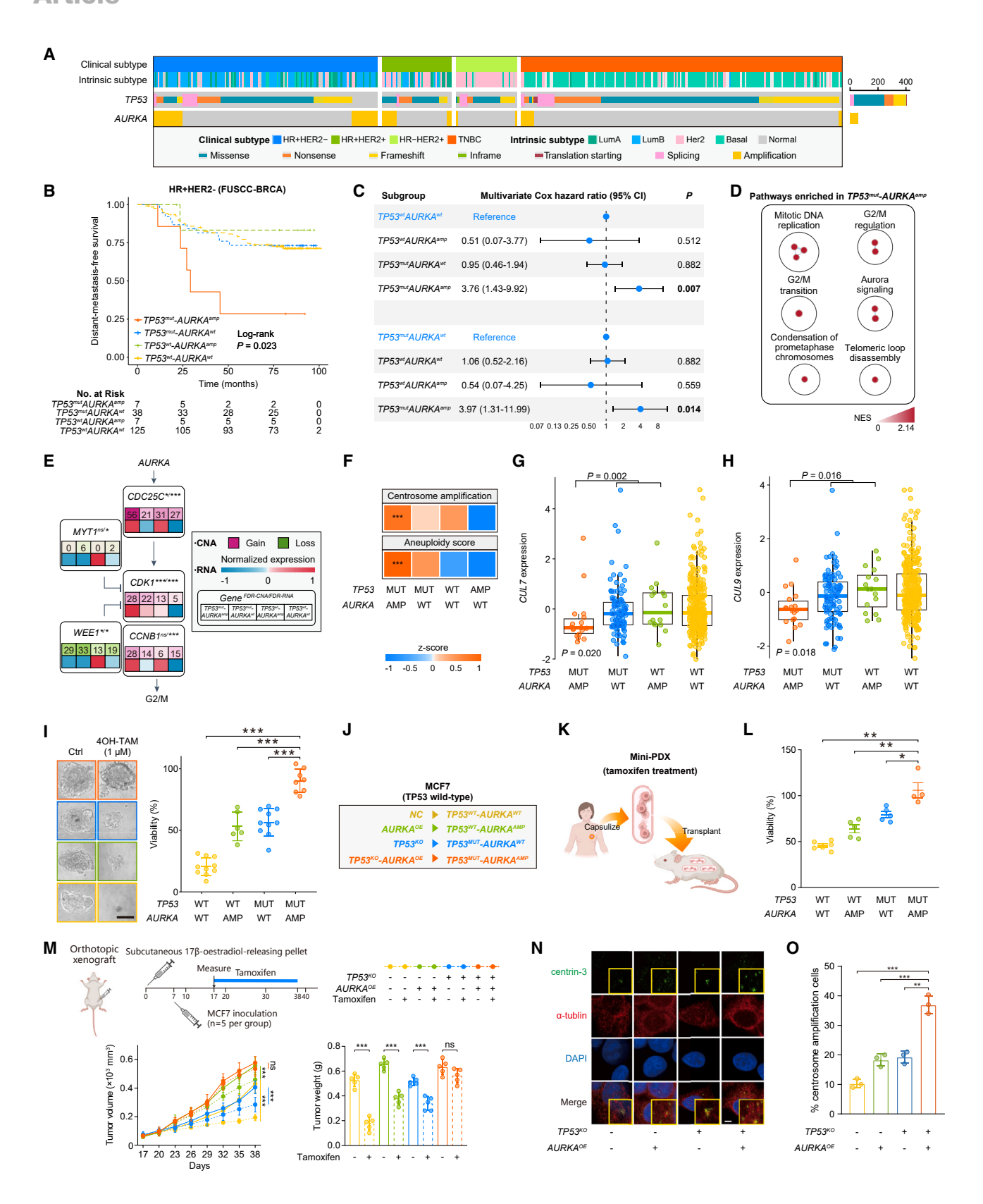
Regarding the co-occurring TP53^{mut}-AURKA^{amp} (Figure 4A), we found that patients with this co-alteration treated with adjuvant tamoxifen experienced a worse prognosis than did those without this co-alteration, as confirmed by both univariate and multivariate analyses (Figures 4B and 4C). Multivariate analysis further revealed a higher risk of distant metastasis in co-altered patients

Figure 3. Associations between co-alterations and patient outcomes

(A) Association between co-alterations and patient survival. Only significant associations are highlighted (p value < 0.05 and FDR < 0.25). Multivariate Cox proportional hazards model was used to adjust for age, histology, tumor size, and lymph node status.

(B) Co-alteration-treatment interactions. Only significant interactions were highlighted (p value < 0.05 and FDR < 0.25). For distant metastasis-free survival (DMFS), a multivariate Cox proportional hazards model with a co-alteration-treatment interaction term was used to adjust for age, histology, tumor size, and lymph node status. For pathologic complete response (pCR), a multivariate logistic regression model with a co-alteration-treatment interaction term was used to adjust for age, histology, tumor size, and lymph node status. For objective response rate (ORR), a multivariate logistic regression model was used to adjust for





(legend on next page)



compared to TP53^{mut}-AURKA^{wt} patients (hazard ratio [HR], 3.97; 95% confidence interval [CI], 1.31–11.99; p = 0.014). We further validated the survival difference in HR+HER2- patients within the METABRIC cohort, where co-alteration carriers demonstrated worse relapse-free survival (Figure S5A).

A subsequent investigation was performed to explore the underlying biological basis. Downstream analysis revealed upregulated G2/M-related pathways, supported by comprehensive transcriptomic, proteomic, and phospho-proteomic data (Figures 4D and S5B-S5D). Further exploration revealed increased CNAs and expression of G2/M transition genes, suggesting potential dysregulation of G2/M phase (Figure 4E). Previous investigations have established the association between centrosome amplification and AURKA expression in the context of P53 deficiency.^{30,31} Consistently, tumors carrying co-occurring *TP53*^{mut}-AURKA amp exhibited higher centrosome amplification score and aneuploidy score (Figure 4F), a recognized manifestation of centrosome amplification.³² Additionally, we observed decreased expression of CUL7 and CUL9 (Figures 4G and 4H), which was associated with aneuploidy as reported in previous studies. 33,34 Since centrosome amplification is a potential contributor to drug resistance, 35,36 these findings suggest that centrosome amplification may be the mechanism underlying TP53mut-AURKAmpinduced endocrine therapy resistance.

Metabolic reprogramming has been identified as a key mechanism of endocrine resistance. To investigate the association between TP53^{mut}-AURKA^{amp} and metabolic dysregulation, network analyses revealed increased perturbations in lipid metabolism rather than polar metabolism (Figures S5E-S5G). We further conducted KEGG metabolic pathway-based differential abundance (DA) analysis between co-altered and single-altered tumors to determine the dysregulated metabolic pathways associated with endocrine resistance. Interestingly, we observed a high DA score for metabolites involved in glycerolipid and sphingolipid metabolism (Figure S5H), pathways associated with cell division, 38 and endocrine resistance.39

To validate the effect of TP53^{mut}-AURKA^{amp} co-alteration on endocrine therapy sensitivity, we performed drug response tests using in vitro cell lines, PDOs, in vivo mini patient-derived xenograft (mini-PDX), and in vivo xenograft models. We first compared tamoxifen sensitivity among PDOs with different coaltered statuses and observed that PDOs harboring the TP53^{mut}-AURKA^{amp} co-alteration exhibited the highest viability, indicating a reduced response to 40H-tamoxifen, followed by TP53^{mut}-AURKA^{wt}, TP53^{wt}-AURKA^{amp}, and TP53^{wt}-AURKA^{wt} PDOs (Figure 4I). Next, we selected the MCF7 cell line as it has a wild-type TP53 genotype. 40 Given that a significant portion of TP53 mutations in our cohort manifest as loss-of-function mutations (Figure 2A), we established MCF7 cell lines with different genetic backgrounds by knockout of endogenous TP53 (TP53^{KO}) and stable overexpression of AURKA (AURKA^{OE}) (Figures 4J and S5I). In vitro viability assays demonstrated decreased sensitivity to tamoxifen in TP53KO-AURKAOE MCF7 cells compared with the control cells (Figure S5J). Consistently, TP53^{mut}-AURKA^{amp} co-altered mini-PDX models presented decreased sensitivity to endocrine therapy (Figures 4K and 4L). In vivo xenograft assays further confirmed larger tumor volumes in TP53KO-AURKAOE models compared to other groups following tamoxifen treatment (Figure 4M). These data collectively suggested an association between co-occurring TP53^{mut}-AURKA^{amp} and decreased tamoxifen responsiveness.

To validate the hypothesis that TP53mut-AURKAmp could induce centrosome amplification, we used immunofluorescence to evaluate centrosome levels in MCF7 cells with different genetic backgrounds. As expected, TP53^{KO}-AURKA^{OE} MCF7 cells, representing TP53^{mut}-AURKA^{amp} genotype, exhibited a higher frequency of centrosome amplification (Figures 4N and 4O). Given previous reports associating centrosome amplification with drug resistance, 35,36 these results suggest that centrosome amplification might underlie TP53mut-AURKAmp-induced resistance to endocrine therapy. While TP53 mutation contributes to CDK2/4 dvsregulation. 41,42 we subsequently treated TP53^{mut}-AURKA^{amp} PDOs with PF3600 (a CDK2/4/6 inhibitor) and alisertib (an

Figure 4. TP53mut-AURKAmp confers endocrine resistance in the HR+HER2- subtype

- (A) Oncoplot showing the co-occurring pattern between TP53 mutation and AURKA amplification.
- (B) Kaplan-Meier curves of distant metastasis-free survival in patients treated with adjuvant tamoxifen harboring different statuses of TP53^{mut}-AURKA^{amp}. p values were estimated and compared based on the log rank test.
- (C) Adjusted hazard ratios and 95% confidence intervals of different statuses of TP53^{mut}-AURKA^{amp} in tamoxifen-treated patients. A multivariate Cox proportional hazards model was adjusted for age, tumor size, and lymph node status.
- (D) Gene set enrichment analysis showing upregulated cell cycle pathways within the TP53^{mut_}AURKA^{amp} tumors.
- (E) Copy number alterations and gene expression in G2/M transition pathway across tumors with different co-alteration statuses.
- (F) Comparison of centrosome amplification (CA20 signature) and aneuploidy scores across different co-alteration statuses. p values were obtained from Kruskal-Wallis test. ***, p < 0.001.
- (G and H) Expression of CUL7 (G) and CUL9 (H) grouped by different co-alteration statuses. Each boxplot presented the median values and 1.5 × interquartile ranges. p values were obtained from logistic regression.
- (I) Representative images of patient-derived organoids (PDOs) with different co-alteration statuses (left) and viability of PDOs with different co-alteration statuses treated with 4OH-TAM. Data are presented as mean \pm SD. Scale bar: 100 μ M. ρ values were obtained from Student's t test. ***, ρ < 0.001.
- (J) MCF7 cell lines with different genetic backgrounds through TP53 knockout (TP53^{KO}) and AURKA overexpression (AURKA^{OE}).
- (K) Scheme of the generation of mini-PDX models for in vivo pharmacological tests.
- (L) Relative viability of HR+HER2- mini-PDX models with tamoxifen treatment normalized to that of vehicle treatment. Data are presented as mean ± SD. p values were obtained from Student's t test. **, p < 0.01; *, p < 0.05.
- (M) Growth curves and tumor weights at the endpoint across tumors with different co-alteration statuses treated with tamoxifen. Data are presented as mean \pm SD. p values were obtained from Student's t test. ***, p < 0.001; ns, not significant.
- (N) Cells stained for microtubules (α-tubulin, red), centrioles (centrin-3, green), and DNA (DAPI, blue) across different co-alteration statuses. Scale bar, 10 μm (O) Histogram showing the fraction of cells with centrosome amplification across different co-alteration statuses. Error bars represent mean ± SD from 3 independent experiments. p values were obtained from Student's t test. ***, p < 0.001; **, p < 0.01. See also Figure S5.



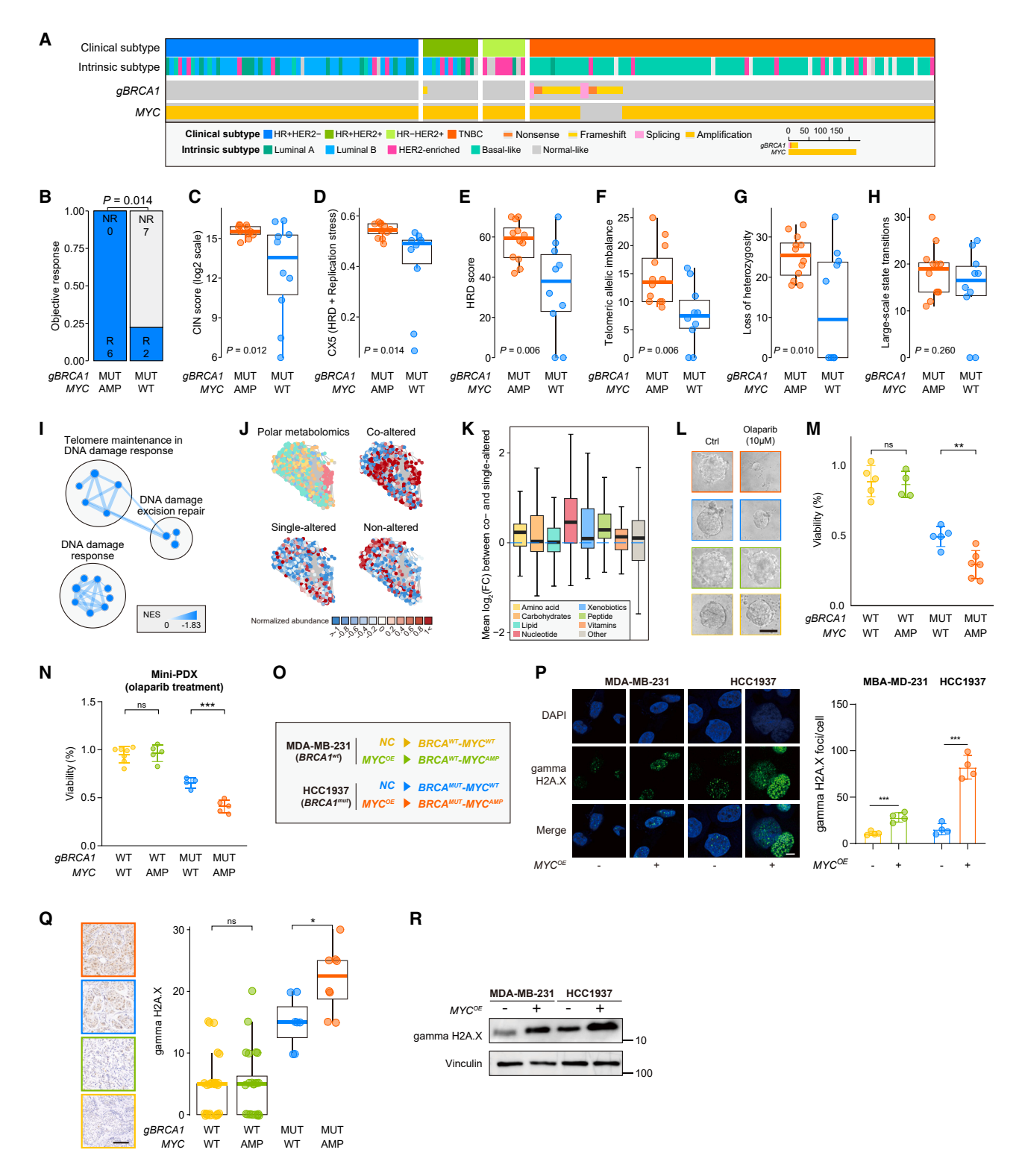


Figure 5. gBRCA1^{mut}-MYC^{amp} suggests potential response to PARP inhibitors

(A) Oncoplot showing the co-occurring pattern between germline BRCA1 mutation and MYC amplification.

(B) Objective response rate stratified by the statuses of gBRCA1^{mut}-MYC^{amp} within HER2-negative patients treated with PARP inhibitor. Multivariate logistic regression was performed to obtain p values after adjusting for age, lines of previous cancer therapy, and hormone receptor status. R, responder; NR, nonresponder.



AURKA inhibitor) to mitigate the effects of TP53 mutation and AURKA amplification, 43 respectively. This treatment substantially inhibited both the growth of TP53mut-AURKAmp PDOs (Figures S5K and S5L) and the occurrence of centrosome amplification in TP53^{KO}-AURKA^{OE} MCF7 cells (Figure S5M).

Taken together, these findings suggest that the co-occurrence of TP53^{mut}-AURKA^{amp} potentially exerts synergistic effects on conferring endocrine resistance through G2/M dysregulation and centrosome amplification.

Co-occurring gBRCA1^{mut}-MYC^{amp} as an indicator of increased genome instability and enhanced response to PARPi

Individuals with germline BRCA1 pathogenic variants have demonstrated promising responses to PARPi therapy. 44 However, variable efficacy within this population highlights the necessity for refined biomarker stratification.⁴⁵ We initially identified co-occurring gBRCA1 mutation and MYC amplification in 56.5% of gBRCA1-mutated patients (Figure 5A). Subsequent analysis focused on PARPi response in gBRCA1-mutated patients with or without MYC amplification, revealing significantly higher ORR in co-altered patients (Figure 5B). Notably, one TNBC patient with chest wall recurrence harboring co-occurring gBRCA1^{mut}-MYC^{amp} experienced notable tumor shrinkage after one cycle of PARPi treatment (Figure S6A). Genetic dependency analysis of the BRCA1^{mut}-MYC^{amp} cancer cell lines also indicated greater sensitivity to the knockout of genes involved in DNA repair (Figure S6B).

Given the divergent efficacy, we further investigated the biological alterations caused by co-occurring MYC amplification in gBRCA1-mutated TNBC. We observed an increased chromosomal instability score (Figure 5C), elevated activity of CX5 copy number signature associated with homologous recombination repair deficiency with replication stress (Figures 5D and S6C), and heightened homologous recombination deficiency (HRD) score in co-altered tumors (Figure 5E). Notably, the telomeric allelic imbalance exhibited the most significant difference in relation to HRD (Figure 5F), followed by loss of heterozygosity (LOH) and large-scale state transitions (Figures 5G and 5H). Transcriptomics analysis further supported downregulated DNA repair pathways (Figure 5I). The collective data suggested elevated DNA damage and decreased repair capacity within *gBRCA1* mut-MYC mp tumors.

We then focused on the dysregulated metabolism associated with co-occurring gBRCA1mut-MYCamp. Network analyses revealed downregulated lipid metabolism (Figure S6D), but not glycerolipid metabolism (Figure S6E). In addition, co-altered tumors exhibited notable difference from single-altered tumors in terms of polar metabolism (Figure 5J), particularly in nucleotide metabolism (Figure 5K). Previous studies have confirmed that dysregulation of nucleotide metabolism is associated with increased DNA damage. 46,47 Metabolic pathway-based DA analysis also supported the upregulated nucleotide metabolism and glycerolipids (Figure S6F). Overall, the co-altered tumors exhibited distinct metabolic patterns.

Subsequently, we validated the impact of co-occurring gBRCA1^{mut}-MYC^{amp} on PARPi sensitivity by employing PDOs and in vivo mini-PDX models. Initial investigations using PDOs revealed reduced viability of gBRCA1^{mut}-MYC^{amp} compared to qBRCA1^{mut}-MYC^{wt} when exposed to olaparib, whereas no significant difference was observed between gBRCA1wt-MYCamp and gBRCA1wt-MYCwt PDOs (Figures 5L and 5M). Consistently, mini-PDX models with gBRCA1^{mut}-MYC^{amp} exhibited increased sensitivity to PARPi (Figure 5N). These data collectively supported the association between co-occurring gBRCA1^{mut}-MY-Camp and improved PARPi sensitivity.

Multi-omics analysis revealed that gBRCA1^{mut}-MYC^{amp} tumors exhibit increased DNA damage, rendering them more susceptible to PARPi. To validate this hypothesis, we selected MDA-MB-231 and HCC1937 cell lines as representative models with wild-type and mutant BRCA1 genotypes, respectively.48 We stably overexpressed MYC (MYC^{OE}) or vector control (Vec^{OE}) in these cell lines to mimic distinct genetic backgrounds (Figures 50 and S6G). Immunofluorescence revealed an elevated level of gamma H2A.X, a marker of double-strand breaks, 49 within the BRCA1 mut-MYC^{OE} HCC1937 cell line (Figure 5P), Immunohistochemical staining for gamma H2A.X further confirmed increased staining intensity in gBRCA1mut-MYCamp tumors (Figure 5Q). Additionally, we observed that MYC overexpression induced DNA damage, as

⁽C-H) Comparisons of chromosomal instability (CIN) score (C), CX5 activity (D), homologous recombination deficiency (HRD) score (E), telomeric allelic imbalance score (F), loss of heterozygosity score (G), and large-scale state transition score (H) between gBRCA1^{mut}-MYC^{amp} and gBRCA1^{mut}-MYC^{wt} TNBCs. Each boxplot presented the median values and 1.5 × interguartile ranges, p values were obtained from logistic regression.

⁽I) Gene set enrichment analysis showing downregulated pathways of DNA damage repair within the gBRCA1^{mut}-MYC^{amp} tumors.

⁽J) Polar metabolomics correlation network based on 669 polar metabolites using Spearman correlation > 0.4 and FDR < 0.05 cutoff. Correlation networks were partitioned and color-coded by a graph-clustering algorithm, and the average quantification of different co-alteration statuses in the correlation networks was presented. Color annotation corresponds to Figure 5K.

⁽K) Log₂ fold changes of the abundances of different categories of polar metabolites in co-altered TNBC tissues as compared with single-altered TNBC tissues. Log₂ fold change value of 0 (the dashed blue line) indicates the same level of polar metabolites abundance between tumor and normal tissues. Each boxplot presented the median values and 1.5 × interquartile ranges.

⁽L) Representative images of PDOs with different co-alteration statuses. Scale bar: 100 µM.

⁽M) Viability of PDOs with different co-alteration statuses treated with olaparib. p values were obtained from Student's t test. Data are presented as mean ± SD. **, p < 0.01; ns, not significant.

⁽N) Relative viability of TNBC mini-PDX models with olaparib treatment, as normalized to vehicle treatment. Data are presented as mean ± SD. p values were obtained from Student's t test. ***, p < 0.001; ns, not significant.

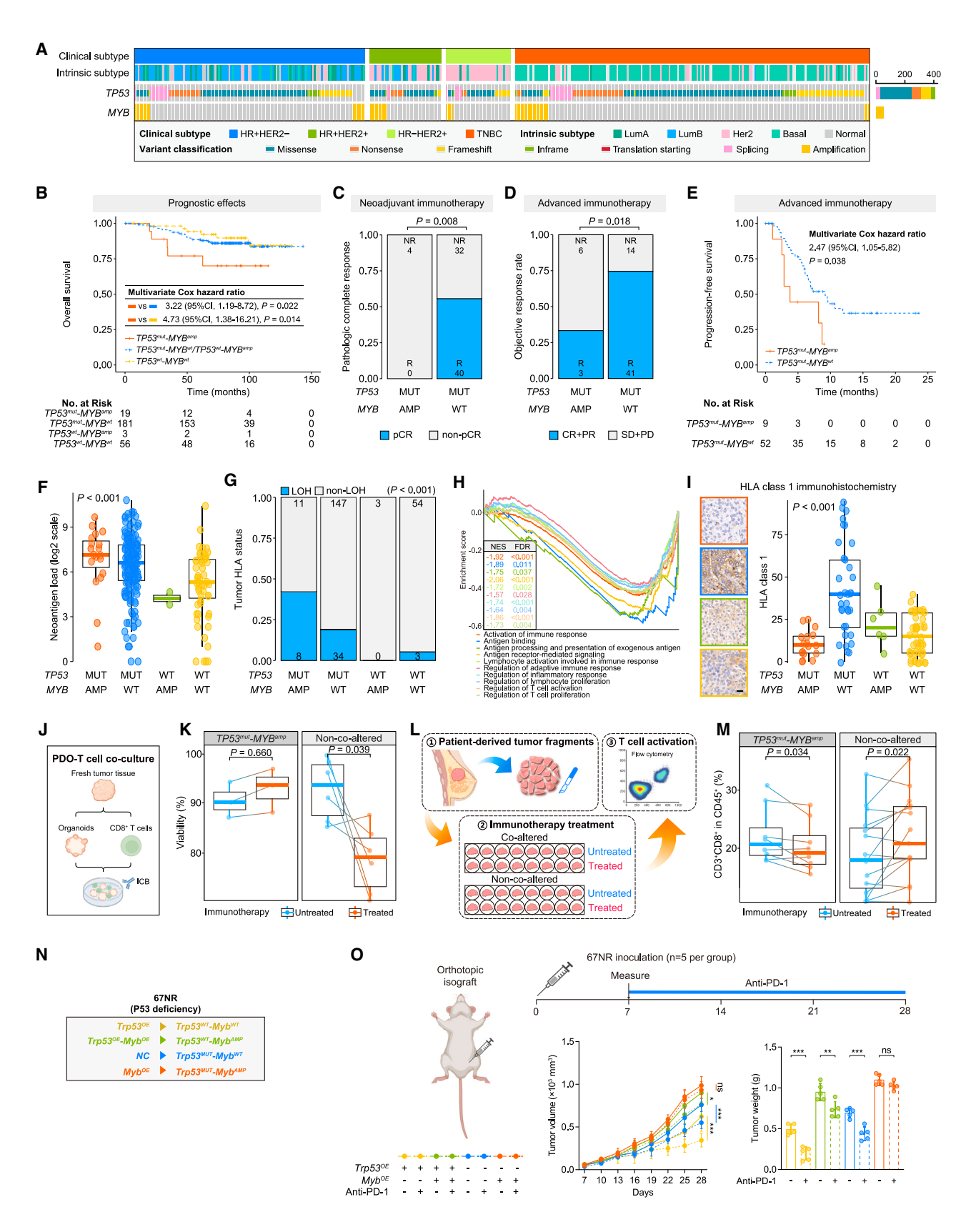
⁽O) HCC1937 (BRCA1^{mut}) and MDA-MB-231 (BRCA1^{wt}) cell lines with different genetic backgrounds by stably overexpressing MYC (MYC^{OE}).

⁽P) Representative images (left) and quantification (right) of immunofluorescence staining of gamma H2A.X (phospho Ser139) (green) foci. Nuclei were stained with DAPI (blue). Data are presented as mean ± SD. Scale bar, 10 μm. p values were obtained via Student's t test. ***, p < 0.001.

⁽Q) Immunohistochemical staining of gamma H2A.X (phospho Ser139). Each boxplot presented the median values and 1.5 × interquartile ranges. Scale bar: 100 μm. p values were obtained via Student's t test. *, p < 0.05; ns, not significant.

⁽R) Western blot analysis of gamma H2A.X (phospho Ser139) in HCC1937 and MDA-MB-231 cell lines with or without MYC overexpression. See also Figure S6.





(legend on next page)





evidenced by increased level of gamma H2A.X (phospho Ser139) (Figure 5R).

Taken together, these findings suggest increased DNA damage, providing a rationale for the enhanced sensitivity to PARPi.

Associations of *TP53*^{mut}-MYB^{amp} with decreased immune infiltration and immunotherapy resistance

Previous studies have highlighted the impact of co-occurring oncogenic alterations on tumor microenvironment (TME) and immunotherapy efficacy. 10 Accordingly, we examined the associations between co-alterations and immunotherapy response. Initial investigation identified the co-occurrence of TP53 mutation and MYB amplification (Figure 6A). As previously stated, compared to non-carriers in TNBC, TP53^{mut}-MYB^{amp} carriers exhibited a worse prognosis (Figure 6B), a lower likelihood of achieving pCR in the neoadjuvant setting (Figure 6C), and a lower ORR in the advanced setting (Figure 6D). Notably, advanced patients harboring co-occurring TP53mut-MYBamp also exhibited poorer progression-free survival when treated with immunotherapy (Figure 6E).

Given the divergent immunotherapy response across different co-alteration statuses, we investigated the underlying biological properties of TP53^{mut}-MYB^{amp} tumors. Interestingly, we observed an increased neoantigen burden within TP53^{mut}-MY-B^{amp} tumors compared to non-co-altered tumors (Figure 6F). However, further analysis revealed a significantly higher incidence of LOH of human leukocyte antigen (HLA-LOH) in TP53^{mut}-MYB^{amp} tumors (Figure 6G). Co-altered tumors further exhibited downregulated pathways related to immune response and antigen presentation (Figure 6H). Consistently, immunohistochemistry confirmed a decreased human leukocyte antigen-l expression in TP53^{mut}-MYB^{amp} tumors (Figure 6I). We also observed increased metabolic dysregulation within the coaltered tumors (Figure S7A). Metabolic pathway-based DA analysis revealed global upregulation of lipid metabolism (Figure S7B), with many metabolites showing a negative correlation with tumor-infiltrating lymphocytes (Figure S7C), particularly sphingolipids, which are recognized indicators of compromised anti-tumor immunity.50 These findings collectively suggest an immunosuppressive TME for TP53^{mut}-MYB^{amp} tumors.

To functionally test our hypothesis, we performed a PDO-T cells co-culture experiment (Figure 6J). Notably, PDOs carrying co-occurring TP53^{mut}-MYB^{amp} exhibited no significant viability changes, whereas non-carriers showed decreased viability after anti-PD-1 antibody treatment (Figure 6K). In addition, we employed PDTFs to evaluate the early immunological response of human tumor tissue to ex vivo PD-1 blockade. After 48 h of incubation with an anti-PD-1 antibody, we profiled the effect of PD-1 blockade on PDTFs with different co-altered statuses using T cell activation markers as readouts (Figures 6L and S7D). Specifically, non-co-altered tumors exhibited increased infiltration and activation of CD3+CD8+ T cells after PD-1 blockade, while TP53^{mut}-MYB^{amp} tumors showed slight decreases (Figures 6M and S7E). To validate the function of TP53^{mut}-MYB^{amp} co-alteration in vivo, we used the BALB/c-derived murine breast cancer cell line 67NR, which is characterized by Trp53 deficiency.⁵¹ Next, we stably overexpressed Trp53 (Trp53^{OE}) or Myb (Myb^{OE}) in 67NR cell lines to mimic different genetic backgrounds (Figures 6N and S7F). The in vivo isograft assay showed that the Vec^{OE}-Myb^{OE} 67NR cell line, mimicking the Trp53^{mut}-Mvb^{amp} genotype, had significantly larger tumor volume than other groups after PD-1 blockade (Figure 6O).

Taken together, these findings provide further support for the association of the TP53^{mut}-MYB^{amp} co-alteration with decreased immune infiltrations and compromised immunotherapy efficacy.

Co-alteration-informed precision treatment strategies to improve patient outcomes

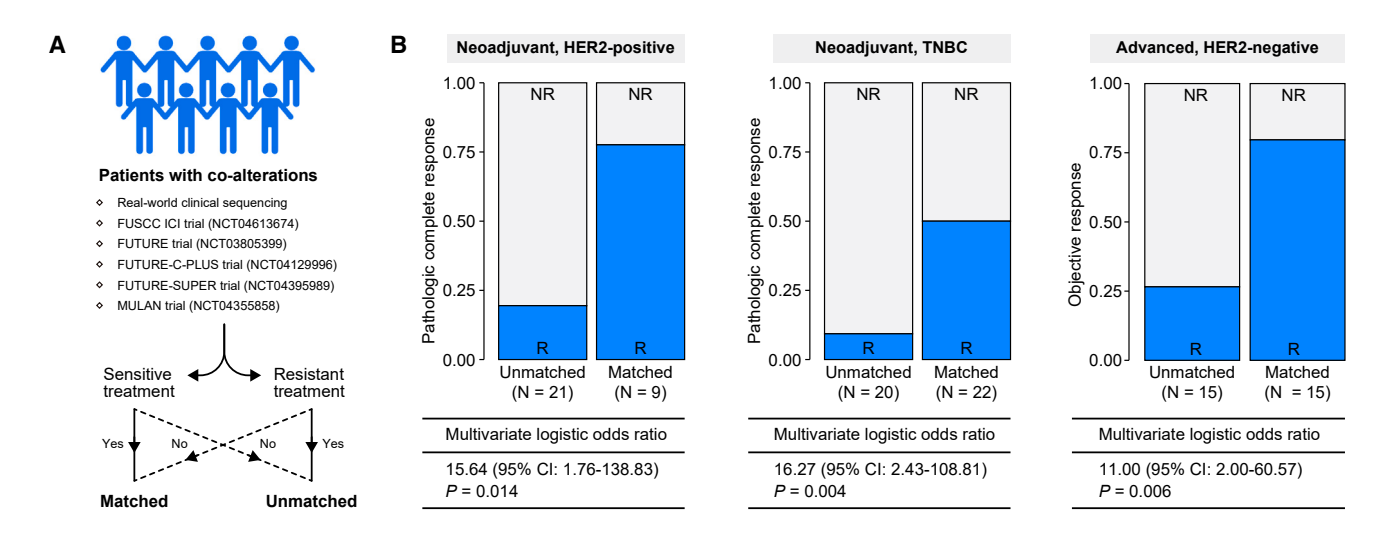
Since we have provided a comprehensive overview of the association of co-alterations with efficacy and biological properties,

Figure 6. Associations of TP53mut-MYBamp with response to immune checkpoint blockade

(A) Oncoplot showing the co-occurring pattern between TP53 mutation and MYB amplification.

- (B) Kaplan-Meier curves of overall survival in patients with TNBC harboring different statuses of TP53^{mut}-MYB^{amp}. Multivariate Cox proportional hazards model was used to obtain hazard ratios and p values, adjusting for confounders of age, histology, tumor size, and lymph node status.
- (C) Pathologic complete response rate stratified by the statuses of TP53^{mut}-MYB^{amp} within TNBC patients treated with neoadjuvant immunotherapy. Multivariate logistic regression was performed to obtain p values after adjusting for age, histology, tumor size, and lymph node status. R, responder; NR, non-responder.
- (D) Objective response rate stratified by the statuses of TP53^{mut}-MYB^{amp} within advanced TNBC patients treated with immunotherapy, p value was obtained from logistic regression model. R, responder; NR, non-responder.
- (E) Kaplan-Meier curves of progression-free survival by the status of TP53^{mut}-MYB^{amp} within the advanced immunotherapy cohort. Cox proportional hazards model was used to estimate the hazard ratio and the corresponding 95% confidence interval
- (F) Levels of neoantigen load grouped by different co-alteration statuses within TNBC. Each boxplot presented the median values and 1.5 x interquartile ranges. p values were obtained from Kruskal-Wallis test.
- (G) Prevalence of human leukocyte antigen loss of heterozygosity (HLA-LOH) across different co-alteration statuses within TNBC. The p value was obtained from multivariate logistic regression model adjusted for age.
- (H) Gene set enrichment analysis showing downregulation of immune-related pathways within the TP53^{mut}-MYB^{amp} tumors.
- (I) Immunohistochemical staining of HLA and H-score quantification. Each boxplot presented the median values and 1.5 × interquartile ranges. Scale bar: 100 um. p values are from Kruskal-Wallis test.
- (J) Schematic diagram of the PDO-T cell co-culture.
- (K) Viability of PDOs with different co-alteration statuses treated with immunotherapy when co-cultured with T cells. Each boxplot presented the median values and $1.5 \times$ interguartile ranges. The p value was obtained from Student's t test.
- (L) Schematic diagram of the patient-derived tumor fragment platform.
- (M) Quantification of CD3+CD8+T cells. Each boxplot presented the median values and 1.5 x interquartile ranges. p values were obtained from paired Student's
- (N) 67NR cell lines with different genetic backgrounds by overexpressing Trp53 (Trp53^{OE}) and Myb (Myb^{OE}).
- (O) Growth curves and tumor weights at the endpoint across tumors with different co-alteration statuses when treated with anti-PD-1. Data are presented as mean \pm SD. p values were obtained from Student's t test. ***, p < 0.001; **, p < 0.01; *, p < 0.05; ns, not significant. See also Figure S7.





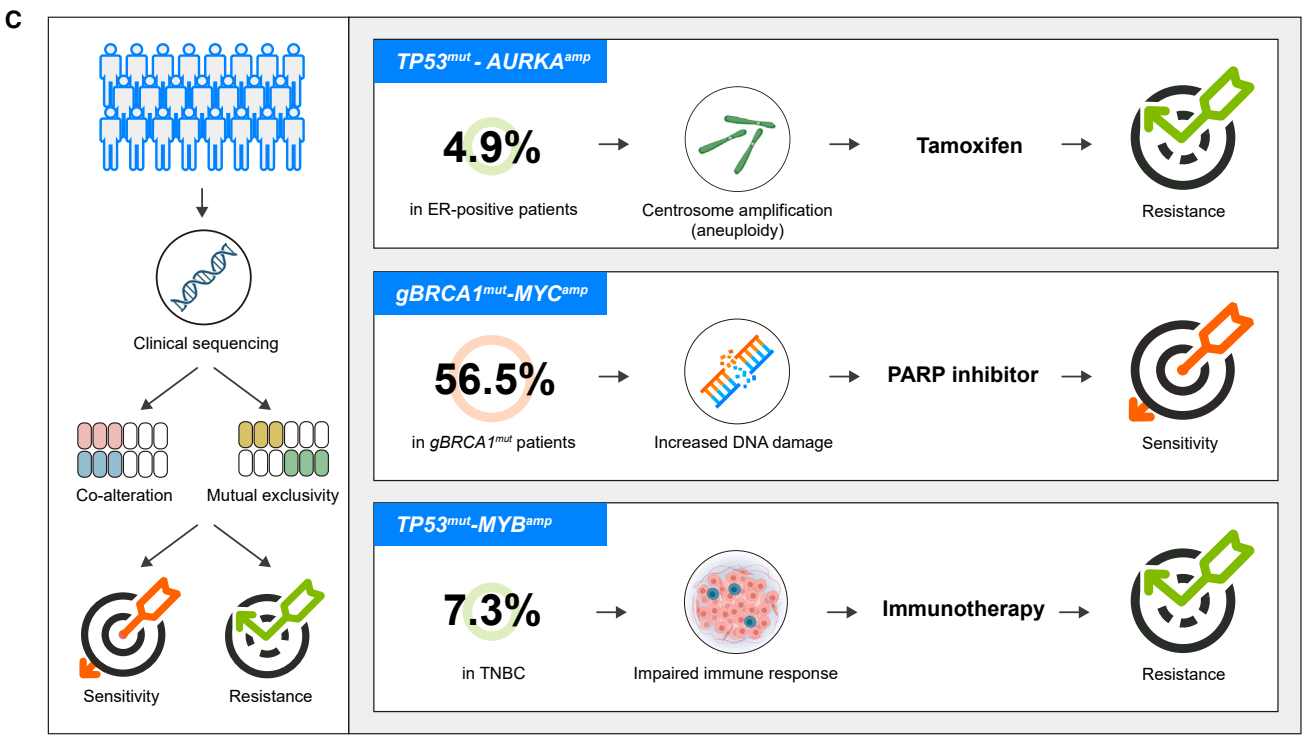


Figure 7. Clinical validation of the co-alteration-informed precision treatment strategies

(A) Schematic diagram of the clinical validation.

(B) Comparison of treatment response between matched and unmatched treatment strategies. R, responder; NR, non-responder.

(C) Summary of underlying biology and therapeutic impacts.

we then evaluated the overall benefit of co-alteration-informed precision treatment in several clinical trial cohorts (Figure 7A). For patients with specific co-alterations, those who received matched therapies showed a significantly better response than did those receiving unmatched treatments (Figure 7B). Further analysis will be conducted when mature survival data become available. These data further highlighted the importance of coalteration-informed precision treatment in improving patient outcomes.

DISCUSSION

Ongoing appreciation of cancer genome and burgeoning application of precision medicine prompted investigations into the impact of co-occurring genomic alterations on both biological properties and therapeutic efficacy. Here, we constructed a comprehensive network of co-occurrence and mutual exclusivity leveraging large-scale multi-omics and clinical sequencing cohorts. Furthermore, we provided an



overview of the therapeutic implications of co-alterations in neoadjuvant, adjuvant, and advanced settings. Additionally, we cataloged the molecular basis of several clinically relevant co-alterations and validated the findings through functional validation. Our findings illuminate the potential of precision treatment strategies informed by co-alterations to enhance patient outcomes (Figure 7C).

While several studies have offered insights into pan-cancer co-occurring and mutually exclusive patterns, these studies did not perform functional validation or investigate the therapeutic implications. Although emerging investigations have identified selected co-occurring events associated with treatment responses in advanced settings,52 our work focused on the impact of co-alterations on clinical outcomes across adjuvant, neoadjuvant, or advanced settings. Multi-dimensional functional validation was further performed to elucidate the functional relationship between co-occurring genomic alterations. Furthermore, our study might be better powered to detect new predictive biomarkers due to a larger sample size of single cancer type, especially in the neoadjuvant cohort. The incorporation of detailed treatment data and comprehensive multi-omics dimensions further enhances the depth and scope of our investigation. These findings should be considered together with existing evidence when determining treatment approaches. Additionally, the concept of co-alteration exhibits notable distinctions and advantages compared to previous investigations. Tumors harboring co-alterations manifest distinctive properties in downstream pathway changes and metabolic reprogramming, suggesting a biological interplay between co-altered driver alterations. Particularly noteworthy is the clinical relevance of the co-alteration concept, presenting potential therapeutic implications. By considering co-alterations, we aim to shape genome-informed treatment decisions, extending beyond the conventional emphasis on individual driver alterations. Overall, our study aims not only to identify robust co-occurring or mutually exclusive events with multifaceted datasets but also, more importantly, to uncover the underlying relationships between these events and clinical outcomes.

To enhance the robustness, we have validated 68.8% of the co-occurrence and mutual exclusivity events. For the missing validation, we acknowledge that the validation differences may be influenced by several factors. First, the FUSCC-ClinSeq, MSK-IMPACT, GENIE-BRCA, and MSK-MetTropism cohorts employed targeted sequencing panels. These panels have inherent limitations, particularly in terms of the number of genes included in the panels and the capability to detect CNAs, thereby leading to failed validation. Additionally, the estimation of co-occurring and mutually exclusive patterns between low-frequency genomic alterations inherently involves randomness across different cohorts. Larger cohorts provide a more robust statistical basis for detecting and validating these events. 13 Finally, differences in clinicopathological compositions and variations in frequency of genomic alterations among diverse cohorts may contribute to the validation discrepancies observed.

We have identified several co-alterations that influence both biology and treatment efficacy of breast cancer. For co-occurring *TP53*^{mut}-AURKA^{amp}, previous studies correlated AURKA

expression negatively with P53 expression⁵³ and associated TP53 mutation and high AURKA expression with an aggressive luminal A subtype.⁵⁴ In addition, our study suggested centrosome amplification as a potential mechanism for endocrine resistance, reinforcing the reported link between AURKA and centrosome amplification observed in P53 deficiency. 30,31 For co-occurring gBRCA1mut-MYCamp, MYC's role in PARPi response remains controversial. Multiple studies have suggested MYC enhances PARPi sensitivity by inducing DNA damage through alternative non-homologous end joining^{55,56} or impairing homologous recombination.⁵⁷ Papp et al. correlated MYC amplification with strong PARPi sensitivity in ovarian cancer. 58 Conversely, Carey et al. reported that MYC knockout resensitized PARPi in TNBC.⁵⁹ However, a clinical trial combining dinaciclib (MYC downregulator) and PARPi showed limited efficacy. 60 Our study emphasized MYC amplification/overexpression over knockout. MYC's role in DNA damage response varies with normal levels promoting repair⁶¹ and excessive expression increasing damage. 55,56,62 Carey et al. suggested MYC promotes RAD51 expression, enhancing DNA damage repair, but efficient repair mediated by RAD51 depends on BRCA1.63,64 Consequently, in the context of germline BRCA1 mutation, cooccurring MYC amplification contributes to elevated DNA damage and decreased repair capacity, thereby enhancing PARPi response. For co-occurring TP53^{mut}-MYB^{amp}, our findings revealed an association with immunotherapy resistance. Despite a high neoantigen load, these tumors exhibit impaired antigen presentation attributed to HLA-LOH. While TP53 mutation has been linked to HLA-LOH, 65 TP53 TP53 tumors showed a higher prevalence of HLA-LOH compared to TP53mut-MYBwt tumors, suggesting a potential functional interaction between TP53 mutation and MYB amplification. This finding underscores the complex interplay between genetic alterations and shaping the immune landscape of these tumors.

Our study has several limitations warranting consideration in future research. First, the three co-alterations emphasized in our study exhibit a relatively low prevalence, limiting the broad clinical impact of our findings. Nonetheless, rather than concentrating on specific co-occurring events, our study highlights that genome-informed treatment decisions should extend beyond individual driver alterations. We will also explore additional genetic interactions that cater to a broader spectrum of breast cancer patients and offer more groundbreaking targets. Second, a larger-scale multi-omics cohort is essential to enhance the statistical power and generalizability of co-occurrence and mutual exclusivity estimation, particularly between germline and somatic alterations. Third, inherent biases exist due to the non-randomized nature of treatment cohorts, necessitating validation of co-alterationtreatment interactions in prospective settings. Finally, the current study lacked in-depth mechanistic investigation. Ongoing experiments aimed to elucidate the functional implications of identified co-alterations.

Overall, we leveraged a large-scale multi-omics cohort and a real-world clinical sequencing cohort to investigate co-occurrence and mutual exclusivity in breast cancer, unveiling their therapeutic implications. These insights may complement ongoing efforts in precision oncology to extend the clinical benefit of genomics-guided precision treatment. With growing



accessibility of tumor genomic sequencing, precision treatment decisions should be based on and beyond single driver alterations.

STAR*METHODS

Detailed methods are provided in the online version of this paper and include the following:

- KEY RESOURCES TABLE
- RESOURCE AVAILABILITY
 - Lead contact
 - Materials availability
 - O Data and code availability
- EXPERIMENTAL MODEL AND SUBJECT DETAILS
 - Patient samples and study cohorts
 - External cohorts
 - Data generation for the FUSCC-BRCA cohort
 - O MS sample processing and data collection for pro-
 - O MS sample processing and data collection for metabolomics
 - O Data generation for FUSCC-ClinSeq cohort
 - List of cancer driver genes
 - Curation of functional variants
 - Pathogenicity prioritization of germline mutations
 - SELECT analysis
 - O Tumor mutation burden estimation
 - O Deciphering mutational signatures and copy number signatures
 - Detection of clustered mutations
 - O Clonality analysis and genome doubling estimation
 - O Estimation of homologous recombination deficiency (HRD) score
 - O Pathway enrichment analysis
 - Network overlavs
 - O Classification of polar metabolites and lipids
 - O KEGG metabolic pathway-based differential abundance analysis
 - O Sensitivity to gene and compound perturbation in breast cancer cell lines
 - O Prognostic effects and co-alteration-treatment interaction analysis
 - Cell culture
 - Plasmids and cloning procedures
 - Lentivirus production and transduction of cell lines
 - Western blotting
 - Immunofluorescence
 - Animal experiments
 - O Drug response test of mini patient-derived xenograft (mini-PDX)
 - O Preparation and culture of patient-derived organoids (PDOs)
 - Drug response test of PDOs
 - O Culture of patient-derived tumor fragments (PDTFs)
 - O PDTF flow cytometry analysis
 - PDO-TILs coculture system and subsequent analyses
 - Immunohistochemistry (IHC) analysis
- QUANTIFICATION AND STATISTICAL ANALYSIS

SUPPLEMENTAL INFORMATION

Supplemental information can be found online at https://doi.org/10.1016/j. ccell.2024.03.006.

ACKNOWLEDGMENTS

This work was supported by grants from the National Key Research and Development Project of China (2021YFF1201300), the National Natural Science Foundation of China (82272822, 82272704, 82341003, 82373184, and 92159301), the Natural Science Foundation of Shanghai (22ZR1479200 and 23ZR1411800), the Shanghai Key Laboratory of Breast Cancer (12DZ2260100), the SHDC Municipal Project for Developing Emerging and Frontier Technology in Shanghai Hospitals (SHDC12021103), the Shanghai Rising-Star Program (23QA1401400), and Youth Talent Program of Shanghai Health Commission (2022YQ012). The funders had no role in the study design, data collection and analysis, decision to publish, or preparation of the manuscript. We also thank Dr. Yan-Cheng Cao for his remarkable efforts in enhancing the visual quality of the figures in our manuscript.

AUTHOR CONTRIBUTIONS

Conceptualization: Y.-Z.J., Z.-M.S., and X.H.; methodology: C.-J.L., X.J., D.M., and Y.O.-Y.; data curation: C.-J.L., D.M., X.J., C.C., Y.O.-Y., Y.-C.P., C.-Z.Z., C.-L.L., F.-L.Q., and L.F.; formal analysis: C.-J.L., X.J., D.M., C.C., Y.O.-Y., and C.-Z.Z.; visualization: C.-J.L. and X.J.; writing - original draft: C.-J.L., X.J., D.M., and Y.O.-Y.; project administration: C.-J.L., X.J., D.M., X.H., Z.-M.S., and Y.-Z.J.; supervision: Y.-Z.J., Z.-M.S., and X.H.

DECLARATION OF INTERESTS

The authors declare no conflicts of interest.

Received: July 26, 2023 Revised: January 16, 2024 Accepted: March 13, 2024 Published: April 8, 2024

REFERENCES

- 1. Wang, D., Liu, B., and Zhang, Z. (2023). Accelerating the understanding of cancer biology through the lens of genomics. Cell 186, 1755–1771.
- 2. AACR Project GENIE Consortium (2017). AACR Project GENIE: Powering Precision Medicine through an International Consortium. Cancer Discov. 7, 818-831.
- 3. Condorelli, R., Mosele, F., Verret, B., Bachelot, T., Bedard, P.L., Cortes, J., Hyman, D.M., Juric, D., Krop, I., Bieche, I., et al. (2019). Genomic alterations in breast cancer: level of evidence for actionability according to ESMO Scale for Clinical Actionability of molecular Targets (ESCAT). Ann. Oncol. 30, 365-373.
- 4. Nolan, E., Lindeman, G.J., and Visvader, J.E. (2023). Deciphering breast cancer: from biology to the clinic. Cell 186, 1708-1728.
- 5. Alvarez, M.J., Subramaniam, P.S., Tang, L.H., Grunn, A., Aburi, M., Rieckhof, G., Komissarova, E.V., Hagan, E.A., Bodei, L., Clemons, P.A., et al. (2018). A precision oncology approach to the pharmacological targeting of mechanistic dependencies in neuroendocrine tumors. Nat. Genet. 50, 979-989.
- 6. Garraway, L.A., and Jänne, P.A. (2012). Circumventing cancer drug resistance in the era of personalized medicine. Cancer Discov. 2, 214-226.
- 7. Skoulidis, F., Byers, L.A., Diao, L., Papadimitrakopoulou, V.A., Tong, P., Izzo, J., Behrens, C., Kadara, H., Parra, E.R., Canales, J.R., et al. (2015). Co-occurring genomic alterations define major subsets of KRAS-mutant lung adenocarcinoma with distinct biology, immune profiles, and therapeutic vulnerabilities. Cancer Discov. 5, 860-877.
- 8. Yates, L.R., Knappskog, S., Wedge, D., Farmery, J.H.R., Gonzalez, S., Martincorena, I., Alexandrov, L.B., Van Loo, P., Haugland, H.K., Lilleng,



- P.K., et al. (2017). Genomic Evolution of Breast Cancer Metastasis and Relapse. Cancer Cell 32. 169–184.e7.
- El Tekle, G., Bernasocchi, T., Unni, A.M., Bertoni, F., Rossi, D., Rubin, M.A., and Theurillat, J.P. (2021). Co-occurrence and mutual exclusivity: what cross-cancer mutation patterns can tell us. Trends Cancer 7, 823–836.
- Skoulidis, F., and Heymach, J.V. (2019). Co-occurring genomic alterations in non-small-cell lung cancer biology and therapy. Nat. Rev. Cancer 19, 495–509.
- Sanchez-Vega, F., Mina, M., Armenia, J., Chatila, W.K., Luna, A., La, K.C., Dimitriadoy, S., Liu, D.L., Kantheti, H.S., Saghafinia, S., et al. (2018). Oncogenic Signaling Pathways in The Cancer Genome Atlas. Cell 173, 321–337.e10.
- Mina, M., Iyer, A., Tavernari, D., Raynaud, F., and Ciriello, G. (2020). Discovering functional evolutionary dependencies in human cancers. Nat. Genet. 52, 1198–1207.
- Mina, M., Raynaud, F., Tavernari, D., Battistello, E., Sungalee, S., Saghafinia, S., Laessle, T., Sanchez-Vega, F., Schultz, N., Oricchio, E., and Ciriello, G. (2017). Conditional Selection of Genomic Alterations Dictates Cancer Evolution and Oncogenic Dependencies. Cancer Cell 32, 155–168.e6.
- Ciriello, G., Cerami, E., Sander, C., and Schultz, N. (2012). Mutual exclusivity analysis identifies oncogenic network modules. Genome Res. 22, 398–406.
- Ciriello, G., Miller, M.L., Aksoy, B.A., Senbabaoglu, Y., Schultz, N., and Sander, C. (2013). Emerging landscape of oncogenic signatures across human cancers. Nat. Genet. 45, 1127–1133.
- Kim, J.W., Botvinnik, O.B., Abudayyeh, O., Birger, C., Rosenbluh, J., Shrestha, Y., Abazeed, M.E., Hammerman, P.S., DiCara, D., Konieczkowski, D.J., et al. (2016). Characterizing genomic alterations in cancer by complementary functional associations. Nat. Biotechnol. 34, 539–546.
- van de Haar, J., Canisius, S., Yu, M.K., Voest, E.E., Wessels, L.F.A., and Ideker, T. (2019). Identifying Epistasis in Cancer Genomes: A Delicate Affair. Cell 177, 1375–1383.
- Carver, B.S., Tran, J., Gopalan, A., Chen, Z., Shaikh, S., Carracedo, A., Alimonti, A., Nardella, C., Varmeh, S., Scardino, P.T., et al. (2009). Aberrant ERG expression cooperates with loss of PTEN to promote cancer progression in the prostate. Nat. Genet. 41, 619–624.
- Dankort, D., Curley, D.P., Cartlidge, R.A., Nelson, B., Karnezis, A.N., Damsky, W.E., Jr., You, M.J., DePinho, R.A., McMahon, M., and Bosenberg, M. (2009). Braf(V600E) cooperates with Pten loss to induce metastatic melanoma. Nat. Genet. 41, 544–552.
- Hanker, A.B., Brown, B.P., Meiler, J., Marín, A., Jayanthan, H.S., Ye, D., Lin, C.C., Akamatsu, H., Lee, K.M., Chatterjee, S., et al. (2021). Co-occurring gain-of-function mutations in HER2 and HER3 modulate HER2/ HER3 activation, oncogenesis, and HER2 inhibitor sensitivity. Cancer Cell 39, 1099–1114.e8.
- Hyman, D.M., Piha-Paul, S.A., Won, H., Rodon, J., Saura, C., Shapiro, G.I., Juric, D., Quinn, D.I., Moreno, V., Doger, B., et al. (2018). HER kinase inhibition in patients with HER2- and HER3-mutant cancers. Nature 554, 189–194.
- Leiserson, M.D.M., Vandin, F., Wu, H.T., Dobson, J.R., Eldridge, J.V., Thomas, J.L., Papoutsaki, A., Kim, Y., Niu, B., McLellan, M., et al. (2015). Pan-cancer network analysis identifies combinations of rare somatic mutations across pathways and protein complexes. Nat. Genet. 47, 106–114.
- Li, X., Dowling, E.K., Yan, G., Dereli, Z., Bozorgui, B., Imanirad, P., Elnaggar, J.H., Luna, A., Menter, D.G., Pilié, P.G., et al. (2022). Precision Combination Therapies Based on Recurrent Oncogenic Coalterations. Cancer Discov. 12, 1542–1559.
- Ulz, P., Heitzer, E., and Speicher, M.R. (2016). Co-occurrence of MYC amplification and TP53 mutations in human cancer. Nat. Genet. 48, 104–106.

- Iorio, F., Knijnenburg, T.A., Vis, D.J., Bignell, G.R., Menden, M.P., Schubert, M., Aben, N., Gonçalves, E., Barthorpe, S., Lightfoot, H., et al. (2016). A Landscape of Pharmacogenomic Interactions in Cancer. Cell 166, 740–754.
- Setton, J., Zinda, M., Riaz, N., Durocher, D., Zimmermann, M., Koehler, M., Reis-Filho, J.S., and Powell, S.N. (2021). Synthetic Lethality in Cancer Therapeutics: The Next Generation. Cancer Discov. 11, 1626–1635.
- Cancer Genome Atlas Network (2012). Comprehensive molecular portraits of human breast turnours. Nature 490, 61–70.
- Curtis, C., Shah, S.P., Chin, S.F., Turashvili, G., Rueda, O.M., Dunning, M.J., Speed, D., Lynch, A.G., Samarajiwa, S., Yuan, Y., et al. (2012). The genomic and transcriptomic architecture of 2,000 breast tumours reveals novel subgroups. Nature 486, 346–352.
- Vasan, N., Razavi, P., Johnson, J.L., Shao, H., Shah, H., Antoine, A., Ladewig, E., Gorelick, A., Lin, T.Y., Toska, E., et al. (2019). Double PIK3CA mutations in cis increase oncogenicity and sensitivity to PI3Kalpha inhibitors. Science 366, 714–723.
- Meraldi, P., Honda, R., and Nigg, E.A. (2002). Aurora-A overexpression reveals tetraploidization as a major route to centrosome amplification in p53-/- cells. EMBO J. 21, 483–492.
- 31. Zhang, D., Shimizu, T., Araki, N., Hirota, T., Yoshie, M., Ogawa, K., Nakagata, N., Takeya, M., and Saya, H. (2008). Aurora A overexpression induces cellular senescence in mammary gland hyperplastic tumors developed in p53-deficient mice. Oncogene 27, 4305–4314.
- 32. Ganem, N.J., Godinho, S.A., and Pellman, D. (2009). A mechanism linking extra centrosomes to chromosomal instability. Nature 460, 278–282.
- 33. Li, Z., Pei, X.H., Yan, J., Yan, F., Cappell, K.M., Whitehurst, A.W., and Xiong, Y. (2014). CUL9 mediates the functions of the 3M complex and ubiquitylates survivin to maintain genome integrity. Mol. Cell 54, 805–819.
- 34. Yan, J., Yan, F., Li, Z., Sinnott, B., Cappell, K.M., Yu, Y., Mo, J., Duncan, J.A., Chen, X., Cormier-Daire, V., et al. (2014). The 3M complex maintains microtubule and genome integrity. Mol. Cell *54*, 791–804.
- Andor, N., Graham, T.A., Jansen, M., Xia, L.C., Aktipis, C.A., Petritsch, C., Ji, H.P., and Maley, C.C. (2016). Pan-cancer analysis of the extent and consequences of intratumor heterogeneity. Nat. Med. 22, 105–113.
- Ippolito, M.R., Martis, V., Martin, S., Tijhuis, A.E., Hong, C., Wardenaar, R., Dumont, M., Zerbib, J., Spierings, D.C.J., Fachinetti, D., et al. (2021). Gene copy-number changes and chromosomal instability induced by aneuploidy confer resistance to chemotherapy. Dev. Cell 56, 2440–2454.e6.
- Hanker, A.B., Sudhan, D.R., and Arteaga, C.L. (2020). Overcoming Endocrine Resistance in Breast Cancer. Cancer Cell 37, 496–513.
- Atilla-Gokcumen, G.E., Muro, E., Relat-Goberna, J., Sasse, S., Bedigian, A., Coughlin, M.L., Garcia-Manyes, S., and Eggert, U.S. (2014). Dividing cells regulate their lipid composition and localization. Cell 156, 428–439.
- 39. Du, T., Sikora, M.J., Levine, K.M., Tasdemir, N., Riggins, R.B., Wendell, S.G., Van Houten, B., and Oesterreich, S. (2018). Key regulators of lipid metabolism drive endocrine resistance in invasive lobular breast cancer. Breast Cancer Res. 20, 106.
- Neve, R.M., Chin, K., Fridlyand, J., Yeh, J., Baehner, F.L., Fevr, T., Clark, L., Bayani, N., Coppe, J.P., Tong, F., et al. (2006). A collection of breast cancer cell lines for the study of functionally distinct cancer subtypes. Cancer Cell 10. 515–527.
- He, G., Siddik, Z.H., Huang, Z., Wang, R., Koomen, J., Kobayashi, R., Khokhar, A.R., and Kuang, J. (2005). Induction of p21 by p53 following DNA damage inhibits both Cdk4 and Cdk2 activities. Oncogene 24, 2929–2943.
- Padmakumar, V.C., Aleem, E., Berthet, C., Hilton, M.B., and Kaldis, P. (2009). Cdk2 and Cdk4 activities are dispensable for tumorigenesis caused by the loss of p53. Mol. Cell Biol. 29, 2582–2593.
- Manfredi, M.G., Ecsedy, J.A., Chakravarty, A., Silverman, L., Zhang, M., Hoar, K.M., Stroud, S.G., Chen, W., Shinde, V., Huck, J.J., et al. (2011). Characterization of Alisertib (MLN8237), an investigational small-molecule

Article



- inhibitor of aurora A kinase using novel in vivo pharmacodynamic assays. Clin. Cancer Res. 17, 7614-7624.
- 44. Bianchini, G., De Angelis, C., Licata, L., and Gianni, L. (2022). Treatment landscape of triple-negative breast cancer - expanded options, evolving needs. Nat. Rev. Clin. Oncol. 19, 91-113.
- 45. Dias, M.P., Moser, S.C., Ganesan, S., and Jonkers, J. (2021). Understanding and overcoming resistance to PARP inhibitors in cancer therapy. Nat. Rev. Clin. Oncol. 18, 773-791.
- 46. Bester, A.C., Roniger, M., Oren, Y.S., Im, M.M., Sarni, D., Chaoat, M., Bensimon, A., Zamir, G., Shewach, D.S., and Kerem, B. (2011). Nucleotide deficiency promotes genomic instability in early stages of cancer development. Cell 145, 435-446.
- 47. Wu, H.-L., Gong, Y., Ji, P., Xie, Y.-F., Jiang, Y.-Z., and Liu, G.-Y. (2022). Targeting nucleotide metabolism: a promising approach to enhance cancer immunotherapy. J. Hematol. Oncol. 15, 45.
- 48. Elstrodt, F., Hollestelle, A., Nagel, J.H.A., Gorin, M., Wasielewski, M., Van Den Ouweland, A., Merajver, S.D., Ethier, S.P., and Schutte, M. (2006). BRCA1 mutation analysis of 41 human breast cancer cell lines reveals three new deleterious mutants. Cancer Res. 66, 41-45.
- 49. Zeng, X., Zhao, F., Cui, G., Zhang, Y., Deshpande, R.A., Chen, Y., Deng, M., Kloeber, J.A., Shi, Y., Zhou, Q., et al. (2022). METTL16 antagonizes MRE11-mediated DNA end resection and confers synthetic lethality to PARP inhibition in pancreatic ductal adenocarcinoma. Nat. Can. (Ott.) 3, 1088-1104.
- 50. Liu, G., Yang, K., Burns, S., Shrestha, S., and Chi, H. (2010). The S1P(1)mTOR axis directs the reciprocal differentiation of T(H)1 and T(reg) cells. Nat. Immunol. 11, 1047–1056.
- 51. Johnstone, C.N., Smith, Y.E., Cao, Y., Burrows, A.D., Cross, R.S.N., Ling, X., Redvers, R.P., Doherty, J.P., Eckhardt, B.L., Natoli, A.L., et al. (2015). Functional and molecular characterisation of EO771.LMB tumours, a new C57BL/6-mouse-derived model of spontaneously metastatic mammary cancer. Dis. Model. Mech. 8, 237-251.
- 52. Liu, R., Rizzo, S., Waliany, S., Garmhausen, M.R., Pal, N., Huang, Z., Chaudhary, N., Wang, L., Harbron, C., Neal, J., et al. (2022). Systematic pan-cancer analysis of mutation-treatment interactions using large real-world clinicogenomics data. Nat. Med. 28, 1656-1661.
- 53. Katayama, H., Sasai, K., Kawai, H., Yuan, Z.M., Bondaruk, J., Suzuki, F., Fujii, S., Arlinghaus, R.B., Czerniak, B.A., and Sen, S. (2004). Phosphorylation by aurora kinase A induces Mdm2-mediated destabilization and inhibition of p53. Nat. Genet. 36, 55-62.
- 54. Ciriello, G., Sinha, R., Hoadley, K.A., Jacobsen, A.S., Reva, B., Perou, C.M., Sander, C., and Schultz, N. (2013). The molecular diversity of Luminal A breast tumors, Breast Cancer Res, Treat, 141, 409–420.
- 55. Caracciolo, D., Scionti, F., Juli, G., Altomare, E., Golino, G., Todoerti, K., Grillone, K., Riillo, C., Arbitrio, M., Iannone, M., et al. (2021). Exploiting MYC-induced PARPness to target genomic instability in multiple myeloma. Haematologica 106, 185-195.
- 56. Nagaria, P.K., Chowdhury, K., Brodie, A., and Rassool, F. (2013). Abstract 1778: C-MYC plays a novel role in driving the error-prone double-strand break repair in triple negative breast cancers. Cancer Res.
- 57. Ning, J.-F., Stanciu, M., Humphrey, M.R., Gorham, J., Wakimoto, H., Nishihara, R., Lees, J., Zou, L., Martuza, R.L., Wakimoto, H., and Rabkin, S.D. (2019). Myc targeted CDK18 promotes ATR and homologous recombination to mediate PARP inhibitor resistance in glioblastoma. Nat. Commun. 10, 2910.
- 58. Papp, E., Hallberg, D., Konecny, G.E., Bruhm, D.C., Adleff, V., Noë, M., Kagiampakis, I., Palsgrove, D., Conklin, D., Kinose, Y., et al. (2018). Integrated Genomic, Epigenomic, and Expression Analyses of Ovarian Cancer Cell Lines. Cell Rep. 25, 2617-2633.
- 59. Carey, J.P.W., Karakas, C., Bui, T., Chen, X., Vijayaraghavan, S., Zhao, Y., Wang, J., Mikule, K., Litton, J.K., Hunt, K.K., and Keyomarsi, K. (2018). Synthetic Lethality of PARP Inhibitors in Combination with MYC

- Blockade Is Independent of BRCA Status in Triple-Negative Breast Cancer, Cancer Res. 78, 742-757.
- 60. Pilié, P.G., Tang, C., Mills, G.B., and Yap, T.A. (2019). State-of-the-art strategies for targeting the DNA damage response in cancer. Nat. Rev. Clin. Oncol. 16, 81-104.
- 61. Luoto, K.R., Meng, A.X., Wasylishen, A.R., Zhao, H., Coackley, C.L., Penn, L.Z., and Bristow, R.G. (2010). Tumor cell kill by c-MYC depletion: role of MYC-regulated genes that control DNA double-strand break repair. Cancer Res. 70, 8748-8759.
- 62. Karlsson, A., Deb-Basu, D., Cherry, A., Turner, S., Ford, J., and Felsher, D.W. (2003). Defective double-strand DNA break repair and chromosomal translocations by MYC overexpression. Proc. Natl. Acad. Sci. USA 100, 9974-9979.
- 63. Cao, M., Lu, K., Liu, G., Zhao, D., and Qi, J. (2020). Biomolecular Interactions of RAD51181-200 with BRCA1846-871 and Mutants and Molecular Docking Approach. Int. J. Pept. Res. Therapeut. 26, 1991-1999.
- 64. Cousineau, I., Abaji, C., and Belmaaza, A. (2005). BRCA1 regulates RAD51 function in response to DNA damage and suppresses spontaneous sister chromatid replication slippage: implications for sister chromatid cohesion, genome stability, and carcinogenesis. Cancer Res. 65, 11384-11391.
- 65. McGranahan, N., Rosenthal, R., Hiley, C.T., Rowan, A.J., Watkins, T.B.K., Wilson, G.A., Birkbak, N.J., Veeriah, S., Van Loo, P., Herrero, J., et al. (2017). Allele-Specific HLA Loss and Immune Escape in Lung Cancer Evolution. Cell 171, 1259-1271.e11.
- 66. Pugh, T.J., Bell, J.L., Bruce, J.P., Doherty, G.J., Galvin, M., Green, M.F., Hunter-Zinck, H., Kumari, P., Lenoue-Newton, M.L., Li, M.M., et al. (2022). AACR Project GENIE: 100,000 Cases and Beyond. Cancer Discov 12, 2044-2057.
- 67. Razavi, P., Chang, M.T., Xu, G., Bandlamudi, C., Ross, D.S., Vasan, N., Cai, Y., Bielski, C.M., Donoghue, M.T., and Jonsson, P. (2018). The Genomic Landscape of Endocrine-Resistant Advanced Breast Cancers. Cancer Cell 34, 427-438.e6.
- 68. Nguyen, B., Fong, C., Luthra, A., Smith, S.A., DiNatale, R.G., Nandakumar, S., Walch, H., Chatila, W.K., Madupuri, R., Kundra, R., et al. (2022). Genomic characterization of metastatic patterns from prospective clinical sequencing of 25,000 patients. Cell 185, 563-575.e11.
- 69. ICGC/TCGA, Pan-Cancer Analysis of Whole Genomes Consortium. (2020). Pan-cancer analysis of whole genomes. Nature 578, 82–93.
- 70. Krug, K., Jaehnig, E.J., Satpathy, S., Blumenberg, L., Karpova, A., Anurag, M., Miles, G., Mertins, P., Geffen, Y., Tang, L.C., et al. (2020). Proteogenomic Landscape of Breast Cancer Tumorigenesis and Targeted Therapy. Cell 183, 1436-1456.e31.
- 71. Tsherniak, A., Vazquez, F., Montgomery, P.G., Weir, B.A., Kryukov, G., Cowley, G.S., Gill, S., Harrington, W.F., Pantel, S., and Krill-Burger, J.M. (2017). Defining a Cancer Dependency Map. Cell 170, 564-576.e16.
- 72. Martincorena, I., Raine, K.M., Gerstung, M., Dawson, K.J., Haase, K., Van Loo, P., Davies, H., Stratton, M.R., and Campbell, P.J. (2017). Universal Patterns of Selection in Cancer and Somatic Tissues. Cell 171, 1029-1041.e21.
- 73. Lawrence, M.S., Stojanov, P., Polak, P., Kryukov, G.V., Cibulskis, K., Sivachenko, A., Carter, S.L., Stewart, C., Mermel, C.H., Roberts, S.A., et al. (2013). Mutational heterogeneity in cancer and the search for new cancer-associated genes. Nature 499, 214-218.
- 74. Wang, K., Li, M., and Hakonarson, H. (2010). ANNOVAR: functional annotation of genetic variants from high-throughput sequencing data. Nucleic Acids Res. 38, e164.
- 75. Chakravarty, D., Gao, J., Phillips, S.M., Kundra, R., Zhang, H., Wang, J., Rudolph, J.E., Yaeger, R., Soumerai, T., Nissan, M., et al. (2017). OncoKB: A Precision Oncology Knowledge Base. JCO Precis Oncol. https://doi.org/10.1200/PO.17.00011.
- 76. Huang, K.L., Mashl, R.J., Wu, Y., Ritter, D.I., Wang, J., Oh, C., Paczkowska, M., Reynolds, S., Wyczalkowski, M.A., Oak, N., et al.





- (2018). Pathogenic Germline Variants in 10,389 Adult Cancers. Cell 173, 355–370.e14.
- Li Q., Wang K. InterVar: Clinical Interpretation of Genetic Variants by the 2015 ACMG-AMP Guidelines. Am J Hum Genet. 2017;100:267-280.
- Ravichandran, V., Shameer, Z., Kemel, Y., Walsh, M., Cadoo, K., Lipkin, S., Mandelker, D., Zhang, L., Stadler, Z., Robson, M., et al. (2019). Toward automation of germline variant curation in clinical cancer genetics. Genet. Med. 21, 2116–2125.
- Alexandrov, L.B., Kim, J., Haradhvala, N.J., Huang, M.N., Tian Ng, A.W., Wu, Y., Boot, A., Covington, K.R., Gordenin, D.A., Bergstrom, E.N., et al. (2020). The repertoire of mutational signatures in human cancer. Nature 578, 94–101.
- Drews, R.M., Hernando, B., Tarabichi, M., Haase, K., Lesluyes, T., Smith, P.S., Morrill Gavarró, L., Couturier, D.L., Liu, L., Schneider, M., et al. (2022). A pan-cancer compendium of chromosomal instability. Nature 606, 976–983.
- McGranahan, N., Favero, F., de Bruin, E.C., Birkbak, N.J., Szallasi, Z., and Swanton, C. (2015). Clonal status of actionable driver events and the timing of mutational processes in cancer evolution. Sci. Transl. Med. 7, 283ra54.
- Carter, S.L., Cibulskis, K., Helman, E., McKenna, A., Shen, H., Zack, T., Laird, P.W., Onofrio, R.C., Winckler, W., Weir, B.A., et al. (2012). Absolute quantification of somatic DNA alterations in human cancer. Nat. Biotechnol. 30, 413–421.
- Van Loo, P., Nordgard, S.H., Lingjærde, O.C., Russnes, H.G., Rye, I.H., Sun, W., Weigman, V.J., Marynen, P., Zetterberg, A., Naume, B., et al. (2010). Allele-specific copy number analysis of tumors. Proc. Natl. Acad. Sci. USA 107, 16910–16915.
- Freed, D., Aldana, R., Weber, J.A., and Edwards, J.S. (2017). The Sentieon Genomics Tools-A fast and accurate solution to variant calling from next-generation sequence data. Preprint at bioRxiv. https://doi.org/ 10.1101/115717.
- Lee, S., Lee, S., Ouellette, S., Park, W.-Y., Lee, E.A., and Park, P.J. (2017). NGSCheckMate: software for validating sample identity in nextgeneration sequencing studies within and across data types. Nucleic Acids Res. 45, e103.
- Wingett, S.W., and Andrews, S. (2018). FastQ Screen: A tool for multigenome mapping and quality control. F1000Res. 7, 1338.
- Andrews, S. (2014). FastQC: A Quality Control Tool for High Throughput Sequence Data. https://www.bioinformatics.babraham.ac.uk/projects/fastqc/
- Okonechnikov, K., Conesa, A., and García-Alcalde, F. (2016). Qualimap
 advanced multi-sample quality control for high-throughput sequencing data. Bioinformatics 32, 292–294.
- Koboldt, D.C., Zhang, Q., Larson, D.E., Shen, D., McLellan, M.D., Lin, L., Miller, C.A., Mardis, E.R., Ding, L., and Wilson, R.K. (2012). VarScan 2: somatic mutation and copy number alteration discovery in cancer by exome sequencing. Genome Res. 22, 568–576.
- Freed, D., Pan, R., and Aldana, R. (2018). TNscope: accurate detection of somatic mutations with haplotype-based variant candidate detection and machine learning filtering. Preprint at bioRxiv. https://doi.org/10. 1101/250647.
- Karczewski, K., and Francioli, L. (2017). The Genome Aggregation Database (gnomAD) (MacArthur Lab).
- Ye, K., Schulz, M.H., Long, Q., Apweiler, R., and Ning, Z. (2009). Pindel: a
 pattern growth approach to detect break points of large deletions and
 medium sized insertions from paired-end short reads. Bioinformatics
 25, 2865–2871.
- McLaren, W., Gil, L., Hunt, S.E., Riat, H.S., Ritchie, G.R.S., Thormann, A., Flicek, P., and Cunningham, F. (2016). The ensembl variant effect predictor. Genome Biol. 17, 122.
- 94. Mermel, C.H., Schumacher, S.E., Hill, B., Meyerson, M.L., Beroukhim, R., and Getz, G. (2011). GISTIC2.0 facilitates sensitive and confident locali-

- zation of the targets of focal somatic copy-number alteration in human cancers. Genome Biol. 12. R41.
- 95. Guo, T., Kouvonen, P., Koh, C.C., Gillet, L.C., Wolski, W.E., Röst, H.L., Rosenberger, G., Collins, B.C., Blum, L.C., Gillessen, S., et al. (2015). Rapid mass spectrometric conversion of tissue biopsy samples into permanent quantitative digital proteome maps. Nat. Med. 21, 407–413.
- Zhu, Y., Weiss, T., Zhang, Q., Sun, R., Wang, B., Yi, X., Wu, Z., Gao, H., Cai, X., Ruan, G., et al. (2019). High-throughput proteomic analysis of FFPE tissue samples facilitates tumor stratification. Mol. Oncol. 13, 2305–2328.
- Shen, B., Yi, X., Sun, Y., Bi, X., Du, J., Zhang, C., Quan, S., Zhang, F., Sun, R., Qian, L., et al. (2020). Proteomic and Metabolomic Characterization of COVID-19 Patient Sera. Cell 182, 59–72.e15.
- Ritchie, M.E., Phipson, B., Wu, D., Hu, Y., Law, C.W., Shi, W., and Smyth, G.K. (2015). limma powers differential expression analyses for RNAsequencing and microarray studies. Nucleic Acids Res. 43, e47.
- 99. Yang, C., Du, X., Hao, R., Wang, Q., Deng, Y., and Sun, R. (2019). Effect of vitamin D3 on immunity and antioxidant capacity of pearl oyster Pinctada fucata martensii after transplantation: Insights from LC-MSbased metabolomics analysis. Fish Shellfish Immunol. 94, 271–279.
- 100. XueKe, G., Shuai, Z., JunYu, L., LiMin, L., LiJuan, Z., and JinJie, C. (2017). Lipidomics and RNA-Seq Study of Lipid Regulation in Aphis gossypii parasitized by Lysiphlebia japonica. Sci. Rep. 7, 1364.
- 101. Dunn, W.B., Broadhurst, D., Begley, P., Zelena, E., Francis-McIntyre, S., Anderson, N., Brown, M., Knowles, J.D., Halsall, A., Haselden, J.N., et al. (2011). Procedures for large-scale metabolic profiling of serum and plasma using gas chromatography and liquid chromatography coupled to mass spectrometry. Nat. Protoc. 6, 1060–1083.
- 102. Benjamin, D., Sato, T., Cibulskis, K., Getz, G., Stewart, C., and Lichtenstein, L. (2019). Calling Somatic SNVs and Indels with Mutect2. Preprint at bioRxiv. https://doi.org/10.1101/861054.
- 103. Shen, R., and Seshan, V.E. (2016). FACETS: allele-specific copy number and clonal heterogeneity analysis tool for high-throughput DNA sequencing. Nucleic Acids Res. 44, e131.
- 104. Poplin, R., Ruano-Rubio, V., DePristo, M.A., Fennell, T.J., Carneiro, M.O., Van der Auwera, G.A., Kling, D.E., Gauthier, L.D., Levy-Moonshine, A., Roazen, D., et al. (2018). Scaling accurate genetic variant discovery to tens of thousands of samples. Preprint at bioRxiv. https://doi.org/10. 1101/201178.
- 105. Sondka, Z., Bamford, S., Cole, C.G., Ward, S.A., Dunham, I., and Forbes, S.A. (2018). The COSMIC Cancer Gene Census: describing genetic dysfunction across all human cancers. Nat. Rev. Cancer 18, 696–705.
- 106. Bailey, M.H., Tokheim, C., Porta-Pardo, E., Sengupta, S., Bertrand, D., Weerasinghe, A., Colaprico, A., Wendl, M.C., Kim, J., Reardon, B., et al. (2018). Comprehensive Characterization of Cancer Driver Genes and Mutations. Cell 173, 371–385.e18.
- 107. Miller, D.T., Lee, K., Chung, W.K., Gordon, A.S., Herman, G.E., Klein, T.E., Stewart, D.R., Amendola, L.M., Adelman, K., Bale, S.J., et al. (2021). ACMG SF v3.0 list for reporting of secondary findings in clinical exome and genome sequencing: a policy statement of the American College of Medical Genetics and Genomics (ACMG). Genet. Med. 23, 1381–1390.
- Rahman, N. (2014). Realizing the promise of cancer predisposition genes. Nature 505, 302–308.
- 109. Degasperi, A., Zou, X., Amarante, T.D., Martinez-Martinez, A., Koh, G.C.C., Dias, J.M.L., Heskin, L., Chmelova, L., Rinaldi, G., Wang, V.Y.W., et al. (2022). Substitution mutational signatures in whole-genome-sequenced cancers in the UK population. Science 376, abl9283.
- 110. Bergstrom, E.N., Luebeck, J., Petljak, M., Khandekar, A., Barnes, M., Zhang, T., Steele, C.D., Pillay, N., Landi, M.T., Bafna, V., et al. (2022). Mapping clustered mutations in cancer reveals APOBEC3 mutagenesis of ecDNA. Nature 602, 510–517.
- 111. Telli, M.L., Timms, K.M., Reid, J., Hennessy, B., Mills, G.B., Jensen, K.C., Szallasi, Z., Barry, W.T., Winer, E.P., Tung, N.M., et al. (2016). Homologous



- Recombination Deficiency (HRD) Score Predicts Response to Platinum-Containing Neoadjuvant Chemotherapy in Patients with Triple-Negative Breast Cancer. Clin. Cancer Res. 22, 3764-3773.
- 112. Hakimi, A.A., Reznik, E., Lee, C.H., Creighton, C.J., Brannon, A.R., Luna, A., Aksoy, B.A., Liu, E.M., Shen, R., Lee, W., et al. (2016). An Integrated Metabolic Atlas of Clear Cell Renal Cell Carcinoma. Cancer Cell 29,
- 113. Xiao, Y., Ma, D., Yang, Y.S., Yang, F., Ding, J.H., Gong, Y., Jiang, L., Ge, L.P., Wu, S.Y., Yu, Q., et al. (2022). Comprehensive metabolomics expands precision medicine for triple-negative breast cancer. Cell Res. 32, 477-490.
- 114. Paik, S., Tang, G., Shak, S., Kim, C., Baker, J., Kim, W., Cronin, M., Baehner, F.L., Watson, D., Bryant, J., et al. (2006). Gene Expression and Benefit of Chemotherapy in Women With Node-Negative, Estrogen Receptor-Positive Breast Cancer. J. Clin. Oncol. 24, 3726-3734.

- 115. Li, C., Sun, Y.D., Yu, G.Y., Cui, J.R., Lou, Z., Zhang, H., Huang, Y., Bai, C.G., Deng, L.L., Liu, P., et al. (2020). Integrated Omics of Metastatic Colorectal Cancer. Cancer Cell 38, 734-747.e9.
- 116. Zhang, F., Wang, W., Long, Y., Liu, H., Cheng, J., Guo, L., Li, R., Meng, C., Yu, S., Zhao, Q., et al. (2018). Characterization of drug responses of mini patient-derived xenografts in mice for predicting cancer patient clinical therapeutic response. Cancer Commun. 38, 60.
- 117. Gong, Y., Ji, P., Yang, Y.S., Xie, S., Yu, T.J., Xiao, Y., Jin, M.L., Ma, D., Guo, L.W., Pei, Y.C., et al. (2021). Metabolic-Pathway-Based Subtyping of Triple-Negative Breast Cancer Reveals Potential Therapeutic Targets. Cell Metabol. 33, 51-64.e9.
- 118. Voabil, P., de Bruijn, M., Roelofsen, L.M., Hendriks, S.H., Brokamp, S., van den Braber, M., Broeks, A., Sanders, J., Herzig, P., Zippelius, A., et al. (2021). An ex vivo tumor fragment platform to dissect response to PD-1 blockade in cancer. Nat. Med. 27, 1250-1261.





STAR***METHODS**

KEY RESOURCES TABLE

REAGENT or RESOURCE	SOURCE	IDENTIFIER
Antibody		
WB: anti-Vinculin	Cell Signaling Technology	Cat# 13901; RRID: AB_2728768
WB: anti-p53 (1C12)	Cell Signaling Technology	Cat# 2524; RRID: AB_331743
WB: anti-Aurora A	Abcam	Cat# ab13824; RRID: AB_300667
WB: anti-c-MYC	Proteintech	Cat# 10828-1-AP; RRID: AB_2148585
WB: anti-c-MYB	Proteintech	Cat# 17800-1-AP; RRID: AB_2148029
WB (also for IHC and IF): anti-gamma H2A.X (phospho S139)	Abcam	Cat# ab22551; RRID: AB_447150
WB: Goat Anti-Rabbit IgG (H + L) HRP	Kigene	Cat# KWB045
WB: Goat Anti-Mouse IgG (H + L) HRP	Kigene	Cat# KI2663
IF: anti-Centrin 3	Abcam	Cat# ab228690
F: anti-Alpha Tubulin	Proteintech	Cat# 66031-1-lg; RRID: AB_11042766
IHC: anti-HLA Class 1 ABC	Abcam	Cat# ab70328; RRID: AB_1269092
IF: Goat Anti-Rabbit IgG (H + L) TRITC-conjugated	Affinity	Cat# S0015; RRID: AB_2844803
IF: Alexa Fluor ®647-conjugated AffiniPure Goat Anti-Mouse IgG (H + L)	Jackson ImmunoResearch	Cat# 115-605-003; RRID: AB_2338902
Ultra-LEAF TM Purified anti-human CD3 Antibody (clone UCHT1)	BioLegend	Cat# 300438; RRID: AB_2749892
Ultra-LEAF TM Purified anti-human CD28 Antibody (clone CD28.2)	BioLegend	Cat# 302934; RRID: AB_2616667
FC: Zombie-NIR	BioLegend	Cat# 423105
FC: AF700 anti-human CD45 (clone: 2D1)	BioLegend	Cat# 368513; RRID: AB_2566373
FC: PE594 anti-human CD3 Antibody (clone: UCHT1)	BioLegend	Cat# 300449; RRID: AB_2563617
FC: PC7 anti-human CD8a (RPA-T8)	BioLegend	Cat# 301012; RRID: AB_314130
FC: FITC anti-ICOS (clone: C398.4A)	BioLegend	Cat# 313505; RRID: AB_416329
FC: PC5.5 anti-human OX40 (clone: Ber-ACT35)	BioLegend	Cat# 350009; RRID: AB_10720986
FC: APC anti-human CD25 (clone: M-A251)	BioLegend	Cat# 356109; RRID: AB_2561976
FC: PE anti-human CD137 (clone: 4B4-1)	BioLegend	Cat# 309803; RRID: AB_314782
Biological samples		
Tumor and normal tissue samples (breast cancer patients)	This study	FUSCC-BRCA FUSCC-ClinSeq
Patient-derived organoids	This study	FUSCCPDO
Patient-derived tumor fragments	This study	FUSCCPDTF
Mini-PDX	This study	FUSCC-miniPDX
Chemicals, peptides, and recombinant proteins		
polybrene	Solarbio	Cat# H8761
puromycin	Invivogen	Cat# 58-58-2
Blasticidin	BasalMedia	Cat# S180J0
Antibody diluent	Kigene	Cat# KWB027
TRIzol Reagent	Invitrogen	Cat# 15596018
PEI MW25000	Polysciences	Cat# 23966
Opti-MEM Reduced Serum Medium, GlutaMAX Supplement	Polysciences	Cat# 51985034
DNase I	Roche	Cat# 10104159001
Collagenase D	Roche	Cat# 11088866001
Collagenase I	Sigma Aldrich	Cat# C0130

(Continued on next page)



Continued		
REAGENT or RESOURCE	SOURCE	IDENTIFIER
TrypLE Express Enzyme	Invitrogen	Cat# 12605036
red blood cell lysis buffer	eBioscience	Cat# 00-4300-54
Leukocyte Activation Cocktail	BD Biosciences	Cat# 550583; RRID: AB_2868893
Cell Staining Buffer	BioLegend	Cat# 420201
Fixation Buffer	BioLegend	Cat# 420801
ntracellular Staining Permeabilization Wash Buffer	BioLegend	Cat# 421002
nVivoMAb anti-mouse PD-1 (clone: RMP1-14)	Bio X Cell	Cat# BE0146; RRID: AB_10949053
nVivoMAb rat IgG2a isotype control (clone: 2A3)	Bio X Cell	Cat# BE0089; RRID: AB_1107769
nVivoPure pH 7.0 Dilution Buffer	Bio X Cell	Cat# IP0070
Tamoxifen	Selleck	Cat# S1238
1-Hydroxytamoxifen (4OH-TAM)	Selleck	Cat# S7827
Alisertib	Selleck	Cat# S1133
PF-06873600	Selleck	Cat# S8816
Dlaparib	Selleck	Cat# S1060
Nivolumab	Selleck	Cat# A2002
Anti-β-Gal-hlgG4	InvivoGen	Cat# S228P
17β-ESTRADIOL	innovrsrch	Cat# SE-121-0.36mg
Matrigel Basement Membrane Matrix	Corning	Cat# 356234
Fc Receptor Blocking Solution	Biolegend	Cat# 422301
Critical commercial assays		
CellTiter-Glo 3D Cell viability assay	Promega	Cat# G9683
Cell Counting Kit-8	Yeasen	Cat# 40203ES92
BCA Protein Assay Kit	Solarbio	Cat# PC0020
Antifade Mounting Medium with DAPI	Beyotime	Cat# P0131
CellTiter Glo Luminescent Cell Viability Assay kit	Promega	Cat# G7571
GTVisionTM III Detection System/Mo&Rb (Including DAB)	Gene Tech	Cat# GK500710
Deposited data		
FUSCC-BRCA	This study	NODE: OEP003358, OEP003049, and OEP000155
FUSCC-ClinSeq	This study	NODE: OEP001027, OEP003469, and OEP004654
TCGA-BRCA	Cancer Genome Atlas Network	https://www.cbioportal.org; Cancer Genome Atlas Network ²⁷
AACR GENIE breast cancer cohort	AACR project	https://genie.cbioportal.org; Pugh et al. ⁶⁶
MSK-IMPACT	Razavi et al. ⁶⁷	https://www.cbioportal.org; Razavi et al. ⁶⁷
MSK-MetTropism	Nguyen et al. ⁶⁸	https://www.cbioportal.org; Nguyenet al. ⁶⁸
PCAWG	PCAWG	https://www.cbioportal.org; ICGC/TCGA PCAWG
METABRIC	Curtis et al. ²⁸	https://www.cbioportal.org; Curtis et al. ²⁸
CPTAC breast cancer cohort	Krug et al. ⁷⁰	https://www.cbioportal.org; Krug et al. ⁷⁰
Cancer Dependency Map (DepMap)	The Broad Institute	https://depmap.org/portal; Tsherniak et al. ⁷¹
Experimental models: Cell lines	חום טוסמט וווסנונענפ	intps://depinap.org/portal, Islieililan et al.
	ATCC	Cot# CDI 2016; DDID; OVCI 2000
Human embryonic kidney cell line HEK293T	ATCC	Cat# CRL-3216; RRID: CVCL_0063
Human breast cancer cell line HCC1937	ATCC	Cat# CRL-2336; RRID: CVCL_0290
Human breast cancer cell line MDA-MB-231	ATCC	Cat# HTB-26; RRID: CVCL_0062
Human breast cancer cell line MCF7	ATCC	Cat# HTB-22; RRID: CVCL_0031
Mouse breast cancer cell line 67NR	Y. Kang Lab	N/A
Experimental models: Organisms/strains		
Female BALB/c mice (5 to 6-week-old)	Chengxi Biotech, Shanghai	N/A
Female BALB/C-NU mice (5 to 6-week-old)	LIDE Biotech, Shanghai	N/A
Female NSG mice (5 to 6-week-old)	Chengxi Biotech, Shanghai	N/A

(Continued on next page)





Continued		
REAGENT or RESOURCE	SOURCE	IDENTIFIER
Oligonucleotides		
sgRNA targeting sequence: TP53: GCATGGGCGGCATGAACCGG	This study	N/A
Recombinant DNA		
pCDH-EF1-FHC	Addgene	Cat# 64874
pMSCV-Blasticidin	Addgene	Cat# 75085
psPAX2	Addgene	Cat# 12260
pCMV-VSV-G	Addgene	Cat# 8454
lentiCRISPR v2	Addgene	Cat# 52961
Ubi-MCS-3FLAG-SV40-EGFP-IRES-puro	GENECHEM Co. Ltd	Cat# GV358
Software and algorithms		
dNdScv	Martincorena et al. ⁷²	https://github.com/im3sanger/dndscv
MutSigCV	Lawrence et al. ⁷³	Lawrence et al. ⁷³
ANNOVAR	Wang et al., 2010 ⁷⁴	https://annovar.openbioinformatics. org/en/latest
annotateMaf	The R Foundation	https://www.r-project.org
oncokb-annotator	Chakravarty et al. ⁷⁵	https://github.com/oncokb/oncokb-annotator
CharGer	Huang et al. ⁷⁶	https://github.com/ding-lab/CharGer
InterVar	Li et al. ⁷⁷	https://github.com/WGLab/InterVar
PathoMan	Ravichandran et al. ⁷⁸	https://pathoman.mskcc.org
SELECT	Mina et al. 12,13	http://ciriellolab.org/select/select.html
SigProfiler tools	Alexandrov et al. ⁷⁹	https://github.com/AlexandrovLab
CINSignatureQuantification	Drews et al. ⁸⁰	https://github.com/markowetzlab/ CINSignatureQuantification
EstimateClonality	McGranahan et al.81	https://bitbucket.org/nmcgranahan/ pancancerclonality/downloads
Absolute	Carter et al. ⁸²	https://github.com/ShixiangWang/DoAbsolute
ASCAT	Van Loo et al. ⁸³	https://github.com/VanLoo-lab/ascat
gprofiler2	The R Foundation	https://www.r-project.org
GSEA	The Broad Institute	https://www.gsea-msigdb.org
EnrichmentMap	Cytoscape APP	https://apps.cytoscape.org/ apps/enrichmentmap
Gephi0.9.3	Gephi	https://gephi.org
survival	The R Foundation	https://www.r-project.org
ComplexHeatmap	Bioconductor	https://bioconductor.org/packages/release/bioc/html/ComplexHeatmap
Flowjo	FlowJo, LLC	https://www.flowjo.com
GraphPad Prism	GraphPad	https://www.graphpad.com/ scientificsoftware/prism
Biorender	N/A	https://biorender.com

RESOURCE AVAILABILITY

Lead contact

Further information and requests for resources and reagents should be directed to and will be fulfilled by the lead contact, Yi-Zhou Jiang (yizhoujiang@fudan.edu.cn).

Materials availability

This study did not generate new unique reagents.



Data and code availability

Raw sequencing data for all datatypes have been deposited in The National Omics Data Encyclopedia (NODE) (http://www.biosino.org/node). The processed multi-omics data and targeted sequencing data have been submitted to NODE by pasting the accession (OEP003358, OEP003049, OEP000155, OEP001027, OEP003469, and OEP004654) into the text search box or through the URL: http://www.biosino.org/node/project/detai/OEP003049, http://www.biosino.org/node/project/detai/OEP003049, http://www.biosino.org/node/project/detai/OEP003049, http://www.biosino.org/node/project/detail/OEP001027, http://www.biosino.org/node/project/detail/OEP001027, http://www.biosino.org/node/project/detail/OEP003469, and http://www.biosino.org/node/project/detail/OEP004654. Targeted sequencing data can also be accessed by visiting the Fudan Data Portal (https://data.3steps.cn/cdataportal/study/clinicalData?id=FUSCC_BRCA_panel_4000). Specific code will be made available upon request to Y.-Z.J.

EXPERIMENTAL MODEL AND SUBJECT DETAILS

Patient samples and study cohorts

Our study incorporated data from several cohorts to discover co-occurrence and mutual exclusivity of genomic alterations and investigate their role in clinical outcomes.

Cohort 1 (FUSCC-BRCA) is a multiomics cohort comprising a total of 873 Chinese breast cancer patients treated at the Department of Breast Surgery at Fudan University Shanghai Cancer Center (FUSCC) between September 2009 and October 2015. Patients within this cohort were included based on the following criteria: 1) females diagnosed with unilateral invasive breast cancer; 2) pathologic examination of tumor specimens by the Department of Pathology at FUSCC, including independently confirmed status of ER, PR, and HER2 by two experienced pathologists based on immunohistochemistry and *in situ* hybridization; a cutoff of \geq 1% positively stained cells was adopted to indicate ER/PR positivity according to the ASCO/CAP guidelines; 3) availability of adequate frozen tissue for further examination. Patients with carcinomas *in situ* or inflammatory breast cancer and patients with *de novo* stage IV breast cancer were excluded.

The last telephone follow-up for patients within this cohort was performed on June 30, 2021, and the median follow-up was 83.2 months (interquartile range, 67.7–92.2 months). The clinical outcomes in our study included distant metastasis-free survival (DMFS) and overall survival (OS). DMFS was defined as the interval from the date of surgery to the first detection of distant metastasis or death from any cause. OS was defined as the interval from the date of surgery to death from any cause. Patients without any events were censored at the time of last follow-up.

Cohort 2 (FUSCC-ClinSeq) is a targeted sequencing cohort. A total of 4,405 consecutive Chinese breast cancer patients who were treated at the Department of Breast Surgery at FUSCC between April 2018 and June 2021 were prospectively included based on the similar inclusion criteria, including the females with unilateral invasive breast cancer whose tumor specimens were subjected to pathologic examination in the Department of Pathology at FUSCC. In addition, the availability of adequate fresh tissue for further examination was required.

We have also initiated several umbrella trials to practice genomics-guided precision treatment in HR + HER2-or triple-negative breast cancer patients, including the FUSCC ICI trial (NCT04613674), FUTURE trial (NCT03805399), the FUTURE-C-PLUS trial (NCT04129996), the FUTURE-SUPER trial (NCT04395989), and the MULAN trial (NCT04355858). Patients' baseline characteristics and treatment outcomes were recorded in a detailed and comprehensive way. These treatment cohorts were also included to evaluate the impact of co-alterations on the treatment efficacy of PARPi or immunotherapies.

Clinicopathological characteristics, the extent of the disease and details of treatment were recorded. All tissue and peripheral blood samples included in this study were obtained after the approval of our research by the FUSCC Ethics Committee, and each patient provided written informed consent.

External cohorts

For validation and further investigation of the biological characteristics of the co-occurrence and mutual exclusivity of genetic events, we collected molecular profiling data of breast cancer and functional readouts of genetic and drug perturbation screening from publicly available repositories (cbioportal.org; genie.cbioportal.org; depmap.org), including The Cancer Genome Atlas (TCGA), MSK-IMPACT, METABRIC, AACR project GENIE Cohort v12.0-public, Clinical Proteomic Tumor Analysis Consortium (CPTAC), MSK-MetTropism, PCAWG, Cancer Cell Line Encyclopedia (CCLE), and The Cancer Interaction Map (DepMap).

Data generation for the FUSCC-BRCA cohort

Sample processing for genomic DNA and total RNA extraction

For quality control (QC), we macro-dissected frozen tumors and tumor cell percentage was confirmed ≥50%. DNA from frozen samples and blood cells was purified using TGuide M24 (Tiangen, Beijing). Genomic DNA purity and quantity were assessed with NanoDrop 2000 (Thermo Scientific, Wilmington) (A260/A280 ratio 1.6–1.9). Total RNA from RNAlater-stored tissues was purified using miRNeasy Mini Kit (Qiagen #217004). RNA integrity was evaluated with Agilent 4200 Bioanalyzer and concentrations determined by NanoDrop ND-8000 (Thermo Fisher Scientific Inc.).

Sample preparation and data generation for RNA sequencing

Libraries were constructed using a Ribo-off rRNA Depletion Kit (Vazyme #N406) for ribosomal RNA depletion, and a VAHTS Universal V8 RNA-seq Library Prep Kit for Illumina (Vazyme #NR605, Vazyme Biotech Co., Ltd. Nanjing) for RNA library construction. This involved reverse-transcribing fragmented RNAs into cDNA, adding 3'-terminal poly(A) modification, and attaching adapters for





PCR library amplification. For library QC, Qubit 4.0 (Thermo Fisher Scientific Inc.) and Agilent 2200 Bioanalyzer (Agilent Inc.) were utilized to assess concentration and fragment size distribution, respectively. Sequencing was carried out on Illumina NovaSeq platforms with paired-end reads of 150 bp.

Raw Illumina data underwent demultiplexing, conversion to FASTQ files, and quantification of adapter and low-quality sequences. HISAT2 mapped sample reads to the hg38 human genome. Expression values in fragments per kilobase of transcript per million mapped reads (FPKM) were obtained through StringTie and Ballgown and genes with FPKM of 0 in over 30% of samples were excluded. **Genomic data analysis of whole-exome sequencing data**

A dataset of 873 tumor/normal pairs was analyzed. Exome-sequenced reads were aligned using BWA-mem, and BAM files were preprocessed with duplicate marking and base quality score recalibration via Sentieon Genomics tools v202010.02.⁸⁴ Quality assessment involved NGSCheckMate, ⁸⁵ FastQ Screen, ⁸⁶ FastQC, ⁸⁷ and Qualimap. ⁸⁸

Somatic variant calling

VarScan2 v2.4.2⁸⁹ (-min-coverage 3 -min-coverage-normal 3 -min-coverage-tumor 3 -min-var-freq 0.08 -p-value 0.10 -somatic-p-value 0.05 -strand-filter 1), TNseq, ⁸⁴ and TNscope ⁹⁰ (Sentieon driver -t -r -algo TNscope -dbsnp -pon) were employed for somatic mutation identification. For raw VarScan2 results, processSomatic and somaticFilter (-min-coverage 10 -min-reads2 2 2 -min-strands2 1 -min-avg-qual 20 -p-value 0.1) were used to extract high-confidence somatic mutations and eliminate clusters of false positives and single-nucleotide variants (SNV) calls near indels. TNseq identified and filtered variants using TNhaplotyper2 (-germline_vcf -pon -algo OrientationBias and -algo ContaminationModel), and TNfilter (-contamination -tumor_segments -orientation_priors). Both TNseq and TNscope utilized a panel of normal (PoN) samples based on 699 normal blood samples, creating two VCF files for identified mutations. Additionally, the location of the population germline resource containing the population allele frequencies obtained from gnomAD⁹¹ were used to filter the raw TNseq results.

To obtain the final variant calls, we first removed spurious variant calls due to sequencing artifacts and employed consensus mutations from at least two out of three callers for somatic mutation identification. Additional bam-readcount filtering (https://github.com/genome/bam-readcount) was applied, considering: 1) variant allele frequency (VAF) \geq 5%; 2) sequencing depth in the region \geq 8; and 3) sequence reads supporting the variant call \geq 4.

Germline variant calling

Pindel⁹² (-c all -x 4 -L -B 0 -M 3 -J hg38_ucsc_centromere.bed) and Sentieon DNAseq Haplotyper⁸⁴ with default parameters were used for germline mutation identification. Only high-confidence variants meeting the following criteria were retained: 1) for SNVs, a minimum of 20x coverage, sequencing depth \geq 5 in the region for the alternative allele, and 20% VAF; 2) for indels, identified by both Haplotyper and Pindel, or Pindel-unique calls with high confidence (at least 30x coverage and 20% VAF). All somatic and germline variant calls were then annotated using both ANNOVAR⁷⁴ and the Ensembl variant effect predictor (VEP). ⁹³

Sample preparation and data generation for copy number alteration (CNA)

The OncoScan CNV Assay Kit (Affymetrix, Santa Clara, CA, USA) was utilized for genome-wide copy number analysis as per the manufacturer's instructions. Each tumor sample, containing 80 ng of DNA, underwent processing. Molecular inversion probes (MIPs) were mixed with sample DNA and annealed at 58°C overnight. The annealed DNA was divided into two equal parts and incubated with AT or GC gap-fill master mixes for ligation. Subsequently, exonuclease treatment removed unincorporated, noncircularized MIPs and remaining genomic templates. Circularized MIPs were linearized with a cleavage enzyme, followed by two successive PCR amplifications. Amplified products were digested with HaellI and Exo enzymes, and small fragments containing specific single-nucleotide polymorphism (SNP) genotypes were hybridized onto arrays.

Arrays underwent washing and staining using a GeneChip Fluidics Station 450 (Affymetrix, Santa Clara), followed by scanning with a GeneChip Scanner 3000 7G (Affymetrix, Santa Clara). Cluster fluorescence intensity was measured to generate a DAT file. Cluster intensity values were automatically calculated using a built-in algorithm from DAT files via GeneChip Command Console software (Affymetrix, Santa Clara), generating a CEL file.

Analysis of SNP array data

Affymetrix OncoScan CNV SNP assays were analyzed with Chromosome Analysis Suite (ChAS) v4.1 software (Thermo Fisher Scientific). A copy number reference model was built using DNA from 23 white blood cell samples and positive controls from the OncoScan CNV Assay Kit. ChAS output was processed with ASCAT (v2.4.3)⁸³ for segmented copy number calls, tumor ploidy, and purity estimates. ASCAT segments were used for log2 ratio calculation by dividing by the total copy number. GISTIC2.0 (v2.0.22)⁹⁴ analyzed gene-level CNV recurrence with specific parameters (-ta 0.2 -td 0.2 -genegistic 1 -smallmem 1 -broad 1 -conf 0.95 -rx 0 -brlen 0.7 -cap 3.5 -armpeel 1 -js 100). Moreover, a group of adjacent normal tissues from 23 patients was used to filter the recurrent germline/potential false-positive calls. Based on the segment output, the probes that suggested gain or loss in at least five patients were used with the help of Integrative Genomics Viewer to constitute a CNV file for removing recurrent germline/potential false-positive calls in GISTIC2.0.

MS sample processing and data collection for proteomics *Proteome analysis*

Proteins were extracted from 1 to 2 mg fresh frozen tissues using 30 μ L lysis buffer (6 M urea, 2 M thiourea, 100 mM triethylammonium bicarbonate) and digested with Lys-C and trypsin (Hualishi, Beijing) assisted by pressure-cycling technology (PCT). TMT-pro 16plex label reagents labeled the peptides, with a common pooled sample as a reference control. TMT-labeled samples were cleaned with a C18 column and fractionated using a Dionex UltiMate3000 HPLC system (Thermo Fisher Scientific, San Jose,



USA). Peptides were consolidated into 30 fractions. Redissolved peptides were analyzed by LC-MS/MS using a DIONEX UltiMate 3000 RSLCnano System coupled with an Orbitrap Exploris 480 mass spectrometer, equipped with a FAIMS Pro in data-dependent acquisition (DDA) mode. LC gradient analysis lasted 60 min, and other LC-MS parameters followed a previous publication.

Database search

The mass spectrometric (MS) data were analyzed by Proteome Discoverer (Version 2.4.1.15, Thermo Fisher) using the human protein data from UniProt (version 15/07/2020, 20368). Normalization was performed against the total peptide amount. Detailed search parameters were referenced in a prior publication. ⁹⁷

Normalization and quality control of proteome data

The primary proteome data matrix underwent log₂ transformation, column-median normalization, and removal of batch effects using the R package limma. Proteins absent in over 30% of samples were excluded. Further quality evaluation methods included correlation between protein and mRNA using Spearman tests and PCA analysis comparing tumor and para-tumor samples. Samples of poor quality were excluded.

MS sample processing and data collection for metabolomics Polar metabolomics detection

Sample quenching and extraction. Twenty-five milligrams of the sample were weighed into an EP tube, and 500 μ L of extraction solution (methanol:acetonitrile:water = 2:2:1) was added. After homogenization (35 Hz for 4 min) and sonication (5 min in an ice-water bath), the cycle was repeated three times. The samples were then incubated for 1 h at -40° C and centrifuged at 12000 rpm for 15 min at 4° C. ⁹⁹ The QC sample was prepared by combining equal aliquots of the supernatants from all samples.

Chromatography separation. LC-MS/MS analyses utilized a UHPLC system (Vanquish, Thermo Fisher Scientific) with a UPLC BEH Amide column (2.1 mm \times 100 mm, 1.7 μ m), connected to a Q Exactive HFX mass spectrometer (Orbitrap MS, Thermo). The mobile phase included 25 mmol/L ammonium acetate and 25 mmol/L ammonia hydroxide in water (pH = 9.75) (A) and acetonitrile (B). The autosampler was set at 4°C, and the injection volume was 2 μ L.

Mass spectrometry. A QE HFX mass spectrometer, known for its MS/MS spectra acquisition in information-dependent acquisition (IDA) mode, was employed with control by Xcalibur software (Thermo). In IDA mode, the software continually assesses the full-scan MS spectrum. ESI source conditions were set as follows: sheath gas flow rate 30 Arb, Aux gas flow rate 25 Arb, capillary temperature 350° C, full MS resolution 60,000, MS/MS resolution 7,500, collision energy 10/30/60 in NCE mode, and spray voltage 3.6 kV (positive) or -3.2 kV (negative).

Data quality control, processing, metabolite identification and data analysis. MS raw data were converted to mzXML using ProteoWizard software (version 3.0.19282) and processed by the XCMS R package (v3.2) for metabolomics, involving peak identification, alignment, extraction, retention time correction, and integration. The BiotreeDB database was utilized for polar metabolites. Internal standards (IS) and QC samples assessed instrument variability. IS-induced variability was calculated by median relative standard deviation (RSD) for added IS in each sample. For QC samples, an equal volume (10 μL) of each sample was mixed and treated independently throughout the detection process, injecting every eight samples. QC distributions in PCA were analyzed to assess instrument and process variability.

To ensure metabolomics data reproducibility, peaks with RSD over 30% in QC samples were filtered out. Remaining peaks were annotated using the R package CAMERA¹⁰⁰ based on retention time and mass-to-charge ratio (m/z) indices. The resulting data matrix included retention time, m/z, and peak intensities. After removing peaks with intensity = 0 in over 50% of samples, peak areas were normalized by isotopically labeled ISs for polar metabolomics.¹⁰¹ To address intra- and interbatch variations, each metabolite peak in subject samples underwent normalization using the LOESS method based on QC samples.¹⁰¹ A LOESS regression model, built on intensity drift in QC samples, predicted and corrected metabolite intensities in subject samples.¹⁰¹

In summary, 669 MS/MS peaks were identified for polar metabolites. Since MS/MS peaks offered clear metabolite identification and greater reliability, our research focused on these peaks.

Lipidomic detection

Sample quenching and extraction. Twenty milligrams of the sample were weighed into an EP tube, followed by sequential addition of 200 μ L water and 480 μ L extract solution (MTBE: MeOH = 5: 1). After 30 s of vortexing, samples were homogenized at 35 Hz for 4 min and sonicated for 5 min in an ice-water bath. This cycle was repeated three times. Samples were then incubated at -40° C for 1 h and centrifuged at 3,000 rpm (RCF = 900 (×g), R = 8.6 cm) for 15 min at 4° C. Three hundred microliters of supernatant was transferred to a fresh tube, and a QC sample was prepared by mixing equal aliquots of all supernatants, dried in a vacuum concentrator at 37° C. Dried samples were reconstituted in 150 μ L of 50% methanol in dichloromethane by sonication for 10 min in an ice-water bath. After centrifugation at 13,000 rpm (RCF = 16200 (×g), R = 8.6 cm) for 15 min at 4° C, $120 \,\mu$ L of supernatant was transferred to a fresh glass vial for LC/MS analysis. Chromatography separation. For lipidomics data collection, UHPLC system (1290, Agilent Technologies) equipped with a Kinetex C18 column (2.1 * 100 mm, 1.7 μ m, Phenomen) was used. Mobile phase A comprised 40% water, 60% acetonitrile, and 10 mmol/L ammonium formate. Mobile phase B comprised 10% acetonitrile and 90% isopropanol, with 50 mL of 10 mmol/L ammonium formate added per 1000 mL of mixed solvent. The elution gradient was as follows: $0 \sim 12.0 \, \text{min}$, $40\% = 100\% \, \text{B}$; $12.0 = 13.5 \, \text{min}$, $100\% \, \text{B}$; $13.7 = 18.0 \, \text{min}$, $40\% \, \text{B}$. The column temperature was 55° C. The autosampler temperature was 4° C, and the injection volume was 3 μ L (pos) or 3 μ L (neg).

Mass spectrometry. Utilizing a QE mass spectrometer in DDA mode controlled by Xcalibur 4.0.27 software (Thermo), we continuously evaluated full-scan MS spectra. ESI source conditions included a sheath gas flow rate of 30 Arb, Aux gas flow rate of 10 Arb,





capillary temperature of 320°C (positive) and 300°C (negative), full MS resolution of 70,000, MS/MS resolution of 17,500, collision energy of 15/30/45 in NCE mode, and spray voltage of 5 kV (positive) or -4.5 kV (negative).

Data processing, metabolite identification and data analysis. MS raw data, converted to mzXML format via ProteoWizard (v3.0.19282) and processed by LipidAnalyzer, underwent peak identification, alignment, extraction, retention time correction, and integration. LipidBlast database facilitated lipid annotation. QC for lipidomics followed procedures akin to polar metabolomics.

In summary, 1,312 MS/MS peaks identified for polar metabolites guided our research due to their clear identification and enhanced reliability.

Data generation for FUSCC-ClinSeq cohort

Prospective sequencing and data generation

Tumor specimens were sent to the Chinese National Human Genome Center at Shanghai (CHGC) for deep-coverage sequencing. Genomic sequencing, utilizing TGuide M24 (Tiangen, Beijing), was conducted on fresh frozen tumor DNA and normal DNA from peripheral blood mononuclear cells. DNA purity and quantity were assessed with NanoDrop 2000 (Thermo Scientific, Wilmington) (A260/A280 ratio 1.6-1.9).

Tumor samples were sequenced using the FUSCC-BC panel (484-gene version 1 and 539-gene version 2), achieving mean depths of coverage at 1000× for tissue and 400× for blood. The panel targets mutations, small insertions/deletions, and copy number alterations. In-house RNA baits, which captured all protein-coding exons of the target genes, were produced from an oligo pool synthesized by Synbio Technologies (Suzhou). The oligo pool converted into double-stranded DNA with integrated T7 promoter sites, transcribed into biotinylated RNA, which was then purified, quantified, and used for target enrichment.

Tumor and matched normal blood samples were concurrently sequenced. Each DNA sample (≥ 10 ng) obtained after SYBR Green quantification underwent fragmentation using a Covaris M220, followed by terminal repair, A-tailing, and adapter ligation with a KAPA HyperPlus kit (Kapa Biosystems) as per the manufacturer's protocol. Subsequently, prepped DNA (750 ng in 3.4 μL) was captured by RNA baits, and the resulting library was purified, amplified with index primers, and quantified using a Multi-Mode Reader (BioTek). Pooled libraries were sequenced on an Illumina HiSeq X TEN platform (Illumina Inc., San Diego). Data collection employed Illumina Real-Time Analysis (RTA), and assembly into fastq files was performed using Illumina Bcl2Fastq2. An in-house bioinformatics pipeline, adhering to the general variant calling procedure, was employed for variant calling and coverage analysis of each capture region. High-quality reads were mapped to the hg19 version of the human reference genome (GRCh37) using the BWA aligner with the BWA-MEM algorithm and default parameters. The Genome Analysis Toolkit (GATK) was applied for local realignment of BAM files at intervals with indel mismatches and recalibration of base quality scores.

Somatic variant calling

GATK (4.0.1.2.0) Mutect2¹⁰² was used to identify somatic mutations. The VCF files were annotated using ANNOVAR. The variants and annotation results were transferred into Excel spreadsheets. A panel of normal (PoN) samples was used to screen out expected germline variations and artifacts for improving specificity. Each alteration identified by the pipeline was manually reviewed to confirm that no false-positive variants were reported. SAMtools (V1.10) and GATK were used to acquire the sequencing quality statistics. The FACETS algorithm¹⁰³ was used to detect gene-level amplification and deletion.

GATK (4.0.1.2.0) Mutect2¹⁰² identified somatic mutations, and ANNOVAR annotated the VCF files. A panel of normal (PoN) samples was used to screen out expected germline variations and artifacts. Manual review ensured no false-positive variants. Sequencing quality statistics were obtained using SAMtools (V1.10) and GATK. The FACETS algorithm detected gene-level amplification and deletion.

Germline variant calling

GATK (4.0.1.2.0) HaplotypeCaller¹⁰⁴ identified germline SNVs and germline indels, retaining high-confidence variants based on criteria: (1) protein-altering or splice site variants; (2) minimum 20x coverage, allelic depth (AD) ≥ 10 for the alternative allele, and $VAF \geq 30\%$.

List of cancer driver genes

We have assembled a list of cancer driver genes based on four sources: 1) the cancer gene list curated by OncoKB (oncokb.org)⁷⁵; 2) genes recorded as oncogenes or tumor suppressor genes (TSGs) by the Cancer Gene Census¹⁰⁵; 3) previously published and functionally validated oncogenic driver genes reported by Bailey et al. 106; 4) the compendium of mutational cancer driver genes from Integrated OncoGenomics (intogen.org).

We also determined the significantly mutated genes (SMG) in the FUSCC-BRCA cohort by using the dNdScv⁷² and MutSigCV.⁷³ Genes with global q < 0.05 by these two methods were retained and intersected. We then took the union set of the cancer driver genes and the SMGs as the cancer genes in the FUSCC-BRCA cohort.

Curation of functional variants

We classified the mutations in cancer genes as functional or neutral based on several criteria. For TSGs, truncating variants, namely frameshift insertions/deletions, nonsense mutations, and essential splicing mutations, were considered putative functional. For both oncogenes and TSGs, hotspot mutations in the Cancer Hotspots database and oncogenic/likely oncogenic mutations in the OncoKB database were retained. Hotspot mutations were annotated using the annotateMaf R package (github.com/taylor-lab/annotateMaf), and



oncogenic mutations were annotated using oncokb-annotator (github.com/oncokb/oncokb-annotator)⁷⁵. In addition, functional variants of the *in silico* prediction based on dbNSFP database version 3.5 were also included. Finally, the list was manually reviewed to remove the variants inconsistent with the role of the genes (for example, inactivating mutations in oncogenes). For the GENIE cohort, the standard Mutation Annotation Format (MAF) file was not available and therefore, we obtained functional mutations defined by cBioPortal, in which variants were classified into putative drivers or variants of uncertain significance based on OncoKB and Cancer Hotspots.

For the functional CNAs, we focused on the alterations of single genes rather than regions of interest (ROIs) since the CNAs at the ROI level are less interpretable and translational. Therefore, we curated the functional CNAs of translational value by reviewing literatures and several knowledge bases, including CIVIc (civicdb.org), JAX-CKB (ckb.jax.org), OncoKB (oncokb.org), PMKB (pmkb. weill.cornell.edu), and MolecularMatch (molecularmatch.com).

Finally, all functional alterations were included in a binary genomic alteration matrix (GAM). Eight GAM files were generated separately for the FUSCC-BRCA, FUSCC-ClinSeq, TCGA-BRCA, MSK-IMPACT, METABRIC, MSK-MetTropism, PCAWG, and GENIE cohorts separately.

Pathogenicity prioritization of germline mutations

Pathogenicity of germline variants were prioritized by CharGer⁷⁶ and InterVar⁷⁷ (github.com/WGLab/InterVar), which are programs designed for automated interpretation of genetic variants based on the ACMG-AMP guidelines. First, we curated a list of cancer predisposing genes by combining the gene lists provided by ACMG,¹⁰⁷ CharGer,⁷⁶ PathoMan,⁷⁸ and Rahman.¹⁰⁸ Germline variants of the cancer predisposition genes classified as pathogenic or likely pathogenic by both InverVar and CharGer were considered deleterious variants. We then reviewed the ClinVar database to manually resolve the inconsistent annotations between these two programs and only included variants classified as pathogenic or likely pathogenic. Additionally, inconsistent annotations were reannotated by a third program, PathoMan, to check the assigned ACMG criteria among all three programs. The inconsistency was addressed by a literature review to determine pathogenicity. Finally, the list was manually reviewed to remove the variants inconsistent with the role of the genes (for example, inactivating mutations in oncogenes). The pathogenic germline variants of the FUSCC-BRCA and FUSCC-ClinSeq cohorts were also incorporated in the corresponding GAM files.

SELECT analysis

The identification co-occurrence or mutual exclusivity of genetic alterations was performed utilizing the SELECT algorithm implemented through the select R package (version 1.6). ^{12,13} SELECT was run with the GAM as the input, allowing all alteration pairs to be analyzed in an unbiased way without any *a priori* assumptions. Only genomic events occurring in at least 5 samples were retained in the GAM file. To estimate the expected background signal, 5,000 random matrices were generated to establish a null model, while the remaining parameters were maintained at their default. Consistency in the analysis was ensured by employing the same parameters for SELECT across all assessments. For enhanced stability and minimization of variance stemming from the seed used for null model generation, SELECT was executed ten times with ten different seeds, and the median SELECT score for each co-occurrence and mutual exclusivity was determined. The threshold of SELECT score significance was determined using the "establish_APC_threshold" function. Co-occurrence and mutual exclusivity were considered significant when their SELECT score exceeded the threshold. For subtype-specific analysis, limitations in sample numbers and alteration events occurring more than five occurrences precluded precise background signal estimation to derive the average sum correction score essential for SELECT score computation. Consequently, in cases with a small number of hypotheses, significance was determined using the *p* value of weighted mutual information (wMI) to identify significant events.

Tumor mutation burden estimation

Tumor mutation burden (TMB) was defined as the number of protein-altering somatic mutations per megabase (muts/Mb) within the coding region of the captured exome (35.618 Mb in our study). Protein-altering mutations were defined as missense, nonsense, nonstop, splice site, translation start site mutations, in-frame and frameshift insertions and deletions.

Deciphering mutational signatures and copy number signatures

Mutational signatures of single-base substitutions (SBS), doublet-base substitutions (DBS), and small insertions and deletions (ID) were extracted separately using SigProfiler, a well-established computational algorithm based on nonnegative matrix factorization (NMF).⁷⁹ First, mutational matrices of *SBS96*, *DBS78*, and *ID83* based on the somatic mutations and their immediate sequence context were created using SigProfilerMatrixGenerator. We then decomposed the mutational matrices of each patient into a known set of reference signatures using SigProfilerSingleSample. The breast cancer-specific reference signatures were sourced from Signal project for SBS and DBS, ¹⁰⁹ while IDs were obtained from the COSMIC Portal.⁷⁹

Copy number signatures were deciphered based on the R package CINSignatureQuantification (version 1.1.2).80

Detection of clustered mutations

Clustered mutations were detected by analyzing the inter-mutational distances (IMD) between SNV-SNV mutations. Specifically, SigProfilerSimulator was first used to calculate an IMD threshold by comparing the mutational patterns of a given sample between real and simulated data to ensure that the clustered events were unlikely to occur by chance. 110 We simulated all somatic mutations in each sample 100 times and determined the IMD threshold with q < 0.1 such that 90% of the mutations below the threshold were





clustered together. Subsequently, SigProfilerClusters with default parameters was employed to partition the clustered mutations from non-clustered mutations and then to further subclassify all clustered mutations into (1) DBS; (2) multi-base substitutions (MBS); (3) diffuse hypermutation (omikli), defined as the mutational events with a length of greater than 1 bp but less than the sample-specific IMD cutoff; and (4) longer events (kataegis).

Clonality analysis and genome doubling estimation

We employed EstimateClonality⁸¹ for estimating the clonality of mutations and utilized Absolute algorithm⁸² for assessing the clonality of copy number alterations. "Same clone" denote instances where either of the co-occurring alterations was a clonal alteration. "Not determined" denote instances both of the co-occurring alterations were classified as subclonal alterations.

We inferred the genome doubling status for each sample by using the R package EstimateClonality based on the copy number profile.

Estimation of homologous recombination deficiency (HRD) score

We calculated the HRD score by summing three independent scores, namely, telomeric allelic imbalance (NtAl), LOH, and large-scale state transition (LST), based on Allele-Specific Copy Number Analysis of Tumors (ASCAT) according to previous studies, ¹¹¹ considering the number of subchromosomal regions with allelic imbalance, the count of LOH regions, and the number of break points between chromosomal regions.

Pathway enrichment analysis

Pathway enrichment analysis was performed and visualized based on the input gene list using the R package gprofiler2. Gene set enrichment analysis (GSEA) was run to identify the enriched pathways and interpret transcriptomic data. Pathways were defined by the gene set file Human_GOBP_AllPathways_no_GO_iea_May_05_2019_symbol.gmt, which is regularly updated and maintained by the Bader laboratory (download.baderlab.org/). GSEA was performed with the gene set size limited to a range between 10 and 300, and 2000 permutations were performed. We then visualized the pathway network based on the EnrichmentMap App (v.3.3) in Cytoscape(v.3.9.1). Pathway clusters were defined and annotated using the Cytoscape app AutoAnnotate (v.1.3.5).

Network overlays

We mapped the co-occurring and mutually exclusive genetic events onto the IntAct protein-protein interactome to confirm that there were specific biological interactions of each co-occurrence and mutual exclusivity of genomic alterations rather than a random statistical estimation. All non-protein nodes were filtered out and only nodes in *Homo sapiens* were kept. IntAct protein-protein interactomes were accessed from the Cytoscape app IntAct.

Classification of polar metabolites and lipids

Using the Kyoto Encyclopedia of Genes and Genomes (KEGG) database, we classified polar metabolites by their associated KEGG metabolic pathways. Eight classifications were determined: lipids, amino acids, carbohydrates, nucleotides, peptides, vitamins and cofactors, xenobiotics and others. Our determination of lipid categories and main classes was based on the LIPID MAPS Structure Database (LMSD). We detected five of eight classical lipid categories (fatty acyls [FA], glycerolipids [GL], glycerophospholipids [GP], sphingolipids [SP], sterol lipids [ST]).

KEGG metabolic pathway-based differential abundance analysis

Differential abundance (DA) scores reflect the tendency of pathways to have higher levels of metabolites than control groups. ^{112,113} A nonparametric DA test (in this study, the Mann–Whitney U test) is performed on all metabolites in a pathway before calculating the score. Once the metabolites were determined to be significantly increased or decreased in abundance, the DA score was calculated as follows: (number of metabolites increased - number of metabolites decreased)/number of measured metabolites within the pathway. DA scores range from -1 to 1. Scoring a pathway as -1 indicated that all metabolites decreased in abundance, while scoring as 1 indicated increased abundance of all metabolites.

Sensitivity to gene and compound perturbation in breast cancer cell lines

We reannotated the MAF file of the cancer cell lines accessed from DepMap using Annovar and applied the same criteria to call the functional mutations for breast cancer cell lines. While for CNAs, we determined the gene-level copy number status according to a previous publication. ¹² For a given co-occurring event between gene *x* and gene *y*, we compared the cell fitness of a specific gene *z* knockout between co- (harboring alterations in both gene *x* and gene *y*) and single-altered (harboring alterations in either gene *x* or gene *y*) cancer cell lines based on the CRISPR screening data accessed from DepMap.

Prognostic effects and co-alteration-treatment interaction analysis

The prognostic value of each co-alteration was evaluated using multivariate Cox proportional hazards models adjusted for baseline confounding factors, including age of diagnosis, tumor histology, tumor size, and lymph node status.



For the analysis of co-alteration-treatment interactions, we employed different endpoints depending on the treatment settings. Distant metastasis-free survival (DMFS), pathologic complete response (pCR), and objective response rate (ORR) were used as separate endpoints to examine the predictive role of co-alterations in the adjuvant, neoadjuvant, and advanced settings, respectively. To evaluate the interaction between co-alterations and treatment on DMFS, we utilized multivariate Cox proportional hazards models that included the baseline confounders. Similarly, for the analysis of pCR and ORR, multivariate logistic regression models were employed, incorporating the baseline confounders. To assess the significance of the co-alteration-by-treatment interaction, the likelihood ratio test was performed. 52,114 This test compared the reduced model, which excluded the co-alteration-by-treatment interaction, with the competing full model that included this interaction. The predictive associations between co-alterations and treatment were concluded if there was a significant (p < 0.05 and FDR < 0.25) co-alteration-by-treatment interaction.

Cell culture

The human breast cancer cell lines MCF7, HCC1937, MDA-MB-231; and human embryonic kidney (HEK) 293T cells were purchased from the American Type Culture Collection and cultured as suggested by ATCC's guidelines. The murine breast cancer cell lines 67NR was a gift from Y. Kang.

Plasmids and cloning procedures

The coding sequences of MYC (NM_002467.6) and Trp53 (NM_011640.3) were cloned into the pCDH-EF1-FHC (Addgene, #64874) vector, and Myb (NM_001198914.1) were cloned into the pMSCV-Blasticidin (Addgene, #75085) vector. The coding sequences of AURKA (NM_003600.4) were cloned into the Ubi-MCS-3FLAG-SV40-EGFP-IRES-puro vector (GENECHEM Co. Ltd, #GV358) to generate the expression vectors. TP53 knockout cell lines were generated using lentiCRISPR v2 plasmids (Addgene, #52961).

Lentivirus production and transduction of cell lines

To produce lentiviral particles, HEK293T cells were seeded into one 10-cm dish and incubated overnight to reach approximately 80% confluence before transfection. Transfection was performed using polyethyleneimine linear (PEI, MW 25,000, Polysciences) according to the recommended protocol. A total of 3.6 mg of psPAX2 (Addgene, #12260) and 1.44 mg of pCMV-VSV-G (Addgene, #8454) were used for each 10-cm dish. After transfection for 8-12 h, the medium was changed to fresh DMEM containing 10% FBS, and the cells were incubated for another 48 h. Culture medium containing the lentiviral particles was collected and filtered through a 0.45-mm filter to remove any remaining cells and debris. The target cells were infected for 24 h with lentiviral particles in the presence of polybrene to establish stable cells.

Western blotting

To prepare whole-cell lysates, the cells were lysed with 1% SDS lysis buffer (50 mM Tris pH 8.1, 1 mM EDTA, 1% SDS, 1 mM fresh dithiothreitol, sodium fluoride, and leupeptin) supplemented with protease and phosphatase inhibitor cocktail, resolved by SDS-PAGE under denaturing conditions and transferred onto 0.45-μm PVDF membranes (Millipore). The membranes were blocked with 10% nonfat milk in 1x TBST (0.9% NaCl, 10 mM Tris-HCl, pH 7.5, containing 0.05% Tween 20) at room temperature (RT) for 1 h and incubated with primary antibody overnight at 4°C followed by incubation with horseradish peroxidase-conjugated secondary antibodies for 1 h at RT. Specific bands were visualized with enhanced chemiluminescence substrate (Millipore) and exposed onto an Amersham Imager 600 (GE Healthcare).

Immunofluorescence

Cells were fixed with 4% paraformaldehyde for 15 min at RT and then blocked with 5% BSA in PBS with 0.3% Triton X-100 (Sigma) at RT for 1 h. Primary antibodies were incubated at 4°C overnight. Antibody dilutions were as follows: gamma H2A.X (Abcam, #ab22551, 1:200), Centrin 3 (Abcam, #ab228690, 1:200), and Alpha Tubulin (Proteintech, #66031-1-lg, 1:200). Then, coverslips were mounted in Antifade Mounting Medium with DAPI (Beyotime). Images were acquired using a Lecia SP5 laser-scanning confocal microscope and LAS AF software (Leica).

Animal experiments

All animal experiments were performed according to protocols approved by the Institutional Animal Care and Use Committee of FUSCC. Five-to-six-week-old female NOD/scid GAMMA (NSG) mice, BALB/c mice were purchased from Shanghai Chenxi Laboratory Animal Care Co. Ltd. and housed under SPF conditions at the animal care facility of the Experimental Animal Center of Fudan University Shanghai Cancer Center. For xenograft models, 8 × 10⁶ MCF7 cells expressing negative control, *TP53^{KO}*, *AURKA^{OE}*, TP53KO-AURKAOE were orthotopically injected directly into the inquinal mammary fat pads of NSG mice in 100 µL of sterile PBS (n = 8 in each group). To allow MCF7 xenograft growth, one week before cell injection a 17β-oestradiol-releasing pellet (Innovrsrch) was inserted in the intra-scapular subcutaneous region. For tamoxifen drug treatment, mice inoculated with MCF7 cells expressing negative control, TP53KO, AURKAOE, TP53KO-AURKAOE were administrated with oral gavage daily to either peanut oil or tamoxifen (45 mg/kg/day in peanut oil). 1×10^6 67NR cells expressing negative control, $Trp53^{OE}$, Myb^{OE} or $Trp53^{OE}$ - Myb^{OE} were orthotopically injected directly into the inquinal mammary fat pads of BALB/c mice in 100 μL of sterile PBS (n = 8 in each group). The isotype rat IgG2a (BE0089, Bio X cell) or anti-PD-1 (BE0146, Bio X cell) (10 mg/kg in InVivoPure pH 7.0 Dilution Buffer per mouse, every 3 days) antibodies were administrated via i.p. injection. Tumor size was measured by caliper twice a week. Tumor volume in mm³





was calculated using the formula: tumor volume = $0.5 \times L \times W^2$, where L is the longest dimension and W is the perpendicular dimension.

Drug response test of mini patient-derived xenograft (mini-PDX)

To rapidly test drug efficacy in vivo, we established mini-PDX models according to previous papers. 115,116 Tumor cells derived from PDO models were harvested and digested into single cells. Cells were then filled into OncoVee capsules (LIDE Biotech, Shanghai, China). Each capsule contained ~2000 cells. Capsules were implanted subcutaneously via a small skin incision with 3 capsules per mouse (5-week-old female BALB/C-NU mouse). Mice bearing mini-PDX capsules were treated with appropriate control or drugs (tamoxifen and olaparib) for 7 continuous days at doses of 45 mg/kg or 50 mg/kg, respectively. All these drugs were prepared by being dissolved in DMSO, PEG300 and Tween-80 solutions. After all capsules were removed from mice, tumor cell proliferation in each capsule was measured using the CellTiter Glo Luminescent Cell Viability Assay kit (G7571, Promega, Madison, WI, US). Tumor cell growth inhibition rate was calculated using the published formula. 116

Preparation and culture of patient-derived organoids (PDOs)

We developed a platform for PDOs storage as previously described. 117 Briefly, fresh breast cancer tissues were minced into small fragments using sterile scalpels. The tissues fragments were then digested and resuspended in 10 mL of TAC buffer. After incubation for 3 min to remove red blood cells, the suspension was passed through a 100 mm cell strainer (Corning). For passaging, the BME was digested using 5 mL of harvesting solution (Trevigen, 3700-100-01) and incubated on ice for 1 h. The resulting organoids were then centrifuged at 350 g for 5 min, washed in digestion buffer, and spun down. Next, 3 mL TrypLE Express (Invitrogen) was added to the organoids, which were incubated at room temperature for 3 min. Mechanical dissociation was performed by pipetting to obtain small cell clusters. Organoids were passaged at a 1:2-3 dilution every 2-3 weeks.

Drug response test of PDOs

For drug treatment of PDOs, organoids in good condition were harvested and digested into single cells. Twenty-five microliters of organoid suspension containing 1 × 10³ to 3 × 10³ cells per well were added to a cell-repellent black surface in clear bottom 384-well plates (Greiner 781976-SIN). The organoids were cultured for an additional 5-6 days before drug treatments. After culturing with drugs for 1 week, the viability of the organoid cells was evaluated using the CellTiter-Glo 3D cell viability assay (Promega, G9683) according to the manufacturer's instructions.

Culture of patient-derived tumor fragments (PDTFs)

Tissue materials that qualified for PDTF cultures were processed by cutting into small tumor fragments of 1-2 mm³ size on ice, as previously reported. 118 Single PDTFs from different regions within a tumor were mixed to ensure uniform representation of the whole tumor. Individual PDTFs were embedded in an artificial extracellular matrix prepared by mixing tumor medium supplemented with 1.1% sodium bicarbonate, 1 mM sodium pyruvate, 1x MEM nonessential amino acids, 2 mM L-glutamine, 10% FBS, 1% penicillin-streptomycin, collagen (1 mg/mL final concentration), and ice-cold Matrigel (4 mg/mL final concentration). A 96-well plate was coated with 40 uL of matrix per well to as a bottom laver and incubated at 37°C for 20-30 min to solidify. A single PDTF per well was placed on top of the pre-solidified matrix, followed by a second layer of 40 μL matrix. The plates were were incubated at 37°C for another 20-30 min to allow solidification. Subsequently, 140 μL of tumor medium supplemented with either nivolumab (20 μg/mL final concentration) or human anti-β-Gal-hlgG4 as a control was added to the top. Each condition was tested with eight PDTFs, and the PDTF cultures were kept at 37°C for 48 h before flow cytometry analysis.

PDTF flow cytometry analysis

Flow cytometry analysis was performed to assess T cell infiltration and activation after culture with either nivolumab or IgG, in order to define the tumor immune environment. The activation of T cell was detected using antibodies from BioLegend, as previous reported. 118 PDTFs for flow cytometry analysis were manually retrieved from the matrix and processed into single-cell suspensions under each experimental condition by enzymatic digestion in a digestion mix consisting of DMEM/F12 medium supplemented with 1% penicillin-streptomycin, 10% BSA, 0.5 μg/mL hydrocortisone, 5 μM Y-27632, 1x insulin, 1 mg/mL collagenase type IV (Worthington), hyaluronidase (Sigma), and Pulmozyme (Sigma), for 1-2 h at 37°C with slow rotation. Digested samples were filtered with a $70~\mu\text{M}$ strainer twice, washed in PBS, and resuspended in $100~\mu\text{L}$ PBS. Fc receptor blocking agent (BioLegend) and Zombie NIR (BioLegend) were added and incubated for 20 min at 4°C. After washing, the cells were resuspended in 50 μL of staining buffer (BioLegend) containing the aforementioned antibodies and incubated for 20 min at 4°C. Following two washes, the cells were suspended in 100 µL of cell staining buffer and subjected to flow cytometry analysis.

PDO-TILs coculture system and subsequent analyses

Primary TNBC tumor tissues were obtained from female patients with breast cancer who underwent surgery at Fudan University Shanghai Cancer Center. PDOs were generated as we described previously. CD8+ TILs from the same tissues were purified by fluorescence-activated cell sorting MoFlo Astrios EQ (Beckman Coulter). PDOs were co-cultured TILs at 1:5 ratio for 2 days before analysis. Nivolumab (10 μg/mL) or vehicle were added to the anti-CD3 and anti-CD28-coated plate with culture medium as indicated. Tumor viability was evaluated via CellTiter-Glo 3D Cell viability assay.



Immunohistochemistry (IHC) analysis

For IHC analysis, paraffin-embedded tissue sections were subjected to the following steps: deparaffinized at 60°C for 20 min, cleared in xylene, and a series of graded alcohols. Hematoxylin and eosin (H&E) staining was performed by staining the slides with Mayer's hematoxylin (Sigma-Aldrich) and 0.1% sodium bicarbonate, followed by counterstaining with eosin Y solution (Sigma-Aldrich). For IHC, slides were heated with saline sodium citrate buffer at 95°C-100°C, then cooled down. Subsequently, the slides were blocked with blocking solution (2% goat serum, 2% BSA, and 0.05% Tween in PBS) at room temperature to block non-specific binding and incubated with a primary antibody diluted in blocking solution at 4° C. Endogenous peroxidase activity was quenched with 0.3% H_2O_2 . Slides were then incubated with a horseradish peroxidase (HRP)-conjugated secondary antibody (GeneTech) at RT. The staining was visualized using a 3,3'-diaminobenzidine substrate (GeneTech). Hematoxylin was used for counterstaining, and a series of graded alcohols were used for dehydration. The positive-staining density was quantified using a computerized imaging system composed of a Leica charge-coupled device DFC420 camera connected to a Leica DM IRE2 microscope (Leic Microsystems Imaging Solutions Ltd). The densities were determined by counting the number of positive cells in 10 high-power field of view, which corresponded to approximately 2 mm². Anti-gamma H2A.X (Abcam, #ab22551, 1:200) and anti-HLA Class 1 ABC (Abcam, #ab70328, 1:2000) were used for the IHC staining in our study.

QUANTIFICATION AND STATISTICAL ANALYSIS

The Mann-Whitney Wilcoxon test or Kruskal-Wallis test were applied to analyze the continuous variables, while Pearson's chi-square test or Fisher's exact test was utilized to compare the categorical variables. Multivariate logistic regression was used to adjust for covariates in the comparison analyses. DMFS was compared by the log rank test. p values were adjusted to the false discovery rate using the Benjamini-Hochberg procedure in multiple comparisons. Ap value of < 0.05 suggested statistical significance unless otherwise stated. All analyses were performed using R version 4.1.1 (https://cran.r-project.org/).